# Thermoelectric and magnetic properties of Cr-doped single crystal $Bi_2Se_3$ – search for energy filtering.

P. Cermak[1], P. Ruleova[1], V. Holy[2,3], J. Prokleska[2], V. Kucek[1], K. Palka[1,4], L. Benes[1], C. Drasar[5*]

[1]*Department of General and Inorganic Chemistry, Faculty of Chemical Technology, University of Pardubice, Studentska 573, 532 10 Pardubice, Czech Republic*

[2]*Department of Condensed Matter Physics, Faculty of Mathematics and Physics, Charles University, Ke Karlovu 3, 121 16 Praha 2, Czech Republic*

[3]*Masaryk University, Department of Condensed Matter Physics and CEITEC, Kotlářská 2, 61137 Brno, Czech Republic*

[4]*Center of Materials and Nanotechnologies - CEMNAT, Faculty of Chemical Technology, University of Pardubice, nam. Cs. legii 565, 530 02 Pardubice, Czech Republic*

[5]*Institute of Applied Physics and Mathematics, Faculty of Chemical Technology, University of Pardubice, Studentska 573, 532 10 Pardubice, Czech Republic*

[*]corresponding author: cestmir.drasar@upce.cz, phone: ±420466036036

**Abstract**

Thermoelectric effects are one of the promising ways to utilize waste heat. Novel approaches have appeared in recent decades aiming to enhance thermoelectric conversion. The theory of energy filtering of free carriers by inclusions ranks is among the latest developed methods. Although the basic idea is clear, experimental evidence of this phenomenon is rare. Based on this concept, we searched suitable systems with stable structures showing energy filtering. Here, we report on the anomalous behavior of Cr-doped single-crystal $Bi_2Se_3$ that indicates energy filtering. The solubility of chromium in $Bi_2Se_3$ was studied, which is the key parameter in the formation process of inclusions. We present recent results on the effect of Cr-doping on the transport coefficients on a wide set of single crystalline samples. Magnetic measurements were used to corroborate the conclusions drawn from the transport and X-ray measurements.

**Key words**

Thermoelectrics; single crystal; transition metal doping; energy filtering; tetradymite

## 1. Introduction

$Bi_2Se_3$, which adopts the tetradymite structure, is one of the constituents of room-temperature thermoelectric (TE) materials [1]. Some of these tetradymite materials have been shown to form diluted magnetic semiconductors (DMS) if they are doped with certain transition metals (TM). A variety of magnetic

ordering has been reported, although the interactions leading to the ordering is still subject to discussion [2-6]. The reason is that there are most likely two or more types of interactions in each TM doped sample. The discovery that these materials are 3D topological insulators (TI) [7-9] has led to renewed attention to doping these materials with magnetic impurities. Among many other materials, $Bi_2Se_3$ is the most promising for electronic applications since its surface states consist of a single Dirac cone, and the material has a reasonably large band gap to guarantee an eventually very low bulk electrical conductivity. The common point to all the works is the spin manipulation. The Ferromagnetism (FM) in Cr-doped [10, 11] or Cr-intercalated [12] $Bi_2Se_3$ has been reported for MBE thin films. Contrarily, an antiferromagnetic (AFM) ordering has been reported for one sample of a Cr-doped $Bi_2Se_3$ single crystal [13]. All reports differ in properties and solubility for the magnetic impurity, and the authors admit that an interaction leading to a magnetic ordering is still unclear and call for further studies. There are profound theoretical calculations reported on the energy formation of defects [e.g., 14], which are very helpful as a guide in terms of tendencies along the periodic table (e.g., V, Cr, Mn, and Fe). Although ref. [14] suggests a slightly negative formation energy of Cr point defects in place of Bi, $Cr_{Bi}$, (i.e., spontaneous formation of such defects), we found the actual concentration of Cr is always lower than the nominal one in our single crystals, which indicates the opposite. Moreover, we found a tendency of clustering when the single crystals are forced to incorporate higher concentrations of Cr during growth from a Cr-rich melt e.g., in Bridgman crystal; Fig. 5 (below) shows an XRF mapping of Cr close to the end (head) of the Bridgman single crystal for x =0.01. In addition, other phases ($Bi_2Cr_4Se_9$) appear for $x \geq 0.02$ in the XRD patterns of our single crystals. This is in accordance with the phase diagram indicating the solubility of Cr in the solid $Bi_2Se_3$ is close to zero, while the liquid state $Bi_2Se_3$ dissolves up to 20% of $Cr_2Se_3$ at 1170 K [15]. Two incongruent compounds are formed in the pseudo-binary phase diagram: the daltonide $Bi_2Cr_4Se_9$, and the berthollide with an approximate composition of $Bi_5Cr_4Se_{13}$. An extraordinary paramagnetism is reported in Bi-Cr-Se ternary misfit-layer compounds based on these two compounds [16].

Following these results, we aim to prepare single-crystal $Bi_{2-x}Cr_xSe_3$ as close to equilibrium as possible for a given temperature to provide a detailed comparison for theoretical and experimental works. The motivation is to provide more insight into the TM-doped tetradymites. There are many uncertainties, including that the equilibrium solubility is lower than that expected from the theoretical predictions. Contrary to some papers [10-13], our results suggest that both AFM and FM ordering exist next to paramagnetism (PM) in this material. Notably, we show that doping with TM might be interesting in terms of TE applications. Namely, TMs are candidates for extra energy filtering of free carriers, which is a way to increase the efficiency of TE materials [17-19]. We think that nano-structuring may explain the extraordinary behavior. We are aware that many questions are not satisfactorily answered, but we hope they can serve as an inspiration.

## 2. Experiment

Single crystals of $Bi_{2-x}Cr_xSe_3$, with nominal x values between 0 and 0.04, were grown by heating stoichiometric mixtures of 5N Bi, Se and $Cr_2Se_3$. The synthesis of $Cr_2Se_3$ was carried out by heating stoichiometric mixtures of 5N purity elements at 1300 K for 7 days in quartz ampoules (all from Sigma-Aldrich).

The crystal growth process involved cooling from 1073 K to 923 K at a rate of 6 K per hour. The crystals were then annealed for 500 hours at 823 K in the same ampoule and then quenched in air. This free melt crystallization (FMC) produces single crystals that are 10–20 mm in length, 3–6 mm wide and up to 3 mm thick. In addition, $Bi_{2-x}Cr_xSe_3$ single crystals were grown using the Bridgman technique (BT) to better understand the behavior of Cr during growth. Contrary to FMC, the BT shows a directional crystallization par excellence. Thus, the liquidus–solidus distribution coefficient of the dopant in the $Bi_2Se_3$ plays an important role. Mostly, the solubility of the doping TM is higher in the liquid phase, as is in case of Cr, and the liquid phase becomes richer in Cr along the direction of crystal growth. Thus, the concentration of chromium increases along the single crystals up to the highest solubility, after which precipitates are eventually formed at a given temperature. The BT produces single crystals up to 60 mm in length, 8 mm wide and 5 mm thick. The orientation of all single crystals was determined using the single-crystal X-ray technique. For the physical property measurements, the FMC specimens with dimensions of 10-15 x 3 x (0.1–0.2) $mm^3$ were cut from the single crystals. The actual doping level and macroscopic homogeneity was examined using XRF mapping with a μ-XRF spectrometer M4 TORNADO (Bruker), Rh-50keV, equipped with polycapillary X-ray optics. To reveal the microscopic homogeneity, we employed energy dispersive X-ray microanalysis (EDX) using scanning electron microscopy (SEM) LYRA 3 (Tescan) equipped with an EDX analyzer Aztec X-Max 20 (Oxford Instruments).

The diffraction patterns (Cu Kα, λ = 1.5418 Å) were recorded on powdered samples using a D8 Advance diffractometer (Bruker AXS, Germany) with a Bragg–Brentano Θ-Θ goniometer (radius 217.5 mm) equipped with a Ni-beta filter and a LynxEye detector. The scan was performed at room temperature from 10 to 90° (2Θ) in 0.01° steps with a counting time of 2 s per step. The lattice parameters were refined using the Le Bail method as implemented in the program FullProf.

High-resolution X-ray diffraction (HR XRD) on single-crystalline $Bi_{2-x}Cr_xSe_3$ samples was carried out on a PaNalytical Expert-Pro diffractometer, equipped with a sealed CuKα tube, primary parabolic multilayer optics, a 2x220Ge single-crystal monochromator, a 3x220Ge analyzer, and a proportional point detector. Using this high-resolution setup, we were able to measure the reciprocal-space distribution of the diffracted intensity with a resolution down to $10^{-4}$ $Å^{-1}$.

The transport parameters include the electrical conductivity $\sigma(i\perp c)$, the Hall coefficient $R_H(B||c)$, and the Seebeck coefficient $S(\Delta T\perp c)$. These parameters were measured in the direction perpendicular to the trigonal axis, *c*, i.e., the electric field and thermal gradients were applied in the basal plane while the magnetic induction vector was parallel to the *c* axis. All parameters were measured over a temperature range from 80 K to 470 K, and a conductive graphite adhesive was used to attach the current leads. Platinum wires (50 μm in diameter) were attached along the sample using thermocompression to measure the voltage drop. The Hall effect and electrical conductivity were examined using a lock-in nano-voltmeter with a 29-Hz excitation and a static magnetic field of 0.6 T. The Seebeck coefficient was determined using the longitudinal steady-state technique with a temperature difference ranging from 3 to 3.5 K. The thermal gradients were measured with

the aid of fine copper-constantan thermocouples. The magnetic properties were investigated using an MPMS apparatus (Quantum Design).

## 3. Results and Discussion

### *3.1. X-ray analysis, XRF analysis, SEM*

A typical X-ray diffraction pattern of $Bi_{2-x}Cr_xSe_3$ obtained for powdered single crystals is shown in Fig. 1. Although all the diffraction peaks can be attributed to the structure of the $Bi_2Se_3$ for x≤0.01, there is clear evidence of additional phases (one peak at 2Θ = 31.3° attributable to both the $Bi_2Cr_4Se_9$ and γ-phase (approximate composition $BiCrSe_3$)) at x=0.03 and x=0.04. This peak is barely detectable for a nominal composition $Bi_{1.98}Cr_{0.02}Se_3$, even for very fine measurements. Thus, the equilibrium solubility of Cr in $Bi_2Se_3$ at 820 K lies below x=0.02. For the TE, this is the nominal concentration over which the micro-precipitates (X-ray detectable) of other phases might form. Thus, the nano-precipitates might form at far lower Cr concentrations depending on the growth kinetics. The lattice parameters of the parent material, *a* = 0.41387 nm and *c* = 2.86303 nm, are in good agreement with those in the database (PDF-4+/ICDD). We observe that the lattice parameters decrease moderately with the increase of the Cr concentration. Table 1 summarizes the lattice parameter values of *a* and *c* for $Bi_{2-x}Cr_xSe_3$. Note that although the actual concentrations of the dopant are small, the crystal radii of the substitutional Cr ($r(Cr^{+3})$ = 0.0755 nm and $r(Cr^{+2})$ = 0.094 nm) are much smaller than that of Bi ($r(Bi^{+3})$ = 0.117 nm) [20]. The slight but measurable drop from doping is close to the experimental errors according to our measurements. Thus, we can observe some solubility of Cr in $Bi_2Se_3$, but we are not able to discuss the solubility of Cr within Vegard´s law.

Figs. 2–4 show the results of the HR XRD diffraction experiments. In Fig. 2, we plotted the symmetric 2theta/omega scan measured on the $Bi_2Se_3$ and $Bi_{2-x}Cr_xSe_3$ (x=0.01) single crystals (points) along with the simulations (lines). Since the sample surface was (0001), the scan trajectory in the reciprocal space crosses the reciprocal-lattice points 000*L*; however, only the diffraction maxima *L*=3,6,… are allowed. The theoretical positions of the maxima are denoted by the vertical dotted lines.

The curves were simulated using the crystallographic data from ref. [21]. The comparison of the measured and simulated curves reveals the excellent quality of the investigated sample; there are neither traces of diffuse scattering from Cr-rich precipitates nor extra peaks from other $Bi_mSe_n$ phases. However, the sensitivity of the HR XRD to the presence of foreign phases is much weaker than that of the powder XRD. The amplitudes of the measured and simulated diffraction maxima 000*L* differ more for the $Bi_{1.99}Cr_{0.01}Se_3$ sample than for the $Bi_2Se_3$. This can be ascribed to the fact that the distances of the basal (0001) planes in the Cr-doped sample differ from the tabulated values, which might be caused by the Cr atoms in the lattice positions and in the vdW gap.

Since the scattering vector in this scan is always perpendicular to the sample surface, this type of scan cannot detect randomly rotated mosaic blocks. To visualize this type of defect, we measured the reciprocal-space maps around the main maximum 000.15 (see [22, 23] for more details) of the $Bi_{1.99}Cr_{0.01}Se_3$ sample and

of a pure $Bi_2Se_3$ single crystal (Fig. 3). Fig. 4(a,b) shows the linear scans extracted from the measured maps along the $Q_x$ and $Q_z$ axes, respectively. The reciprocal-space maps demonstrate the good crystal quality. The horizontal diffuse elongation of the diffraction maxima can be observed in both the $Bi_{1.99}Cr_{0.01}Se_3$ and $Bi_2Se_3$ samples, which is caused by randomly rotated mosaic blocks. Nevertheless, in both investigated samples, the main maximum is approximately 100 times higher than the diffuse peak. From this fact, we conclude that the majority of the sample volume is not rotated, and the rotated blocks make up less than approximately 1 percent of the total irradiated volume. Detailed inspection of the data reveals two interesting features that are visible mainly in the $Q_x$-scans from Fig. 4(a). The curve of sample $Bi_{1.99}Cr_{0.01}Se_3$ always contains a rather sharp side maximum (blue arrow in Fig. 4(a)). This maximum most likely stems from a misoriented large mosaic block. The degree of the block misorientation can be estimated as 0.26° with respect to the surrounding crystal matrix, and its lateral size can be compared to the coherence width of the primary X-ray beam, i.e., 0.5–1.0 μm. A similar feature can be found on the $Q_x$-scan of $Bi_2Se_3$ [red arrow in Fig. 4(b)]. The interpretation of this effect is complicated and might be caused by many misoriented blocks (misorientation on the order of 1 deg). Thus, the blocks are probably very small in the lateral direction (tens of nm). Fig. 4(b) shows the vertical ($Q_z$-) scans extracted from Fig. 3. The $Q_z$-scans of both samples are very similar, and their widths are comparable to the experimental resolution. This finding indicates that the distances of the (0001) basal planes in the rotated mosaic blocks and in the main crystal are the same, i.e., the local lattices of the blocks are only rotated and not strained. The physical nature of these blocks is not clear. For example, they can be created by laterally small faults in the stacking of the Bi-Se basal atomic planes (stacking faults or twins). The effect of the dislocations is less likely, since no deformation of the block lattices was observed.

Fig. 5 shows the XRF mapping (≈ 100 μm mean penetration depth) of the cleaving plane of the BT single crystals. In fact, we observed random cluster formation in all studied single crystals for x≥0.01, although the occurrence decreases markedly with the drop of the Cr content. Furthermore, the increasing concentration of Cr is apparent towards the end of the BT crystal, which indicates a higher solubility of Cr in liquid rather than the solid phase. In fact, the actual solubility of Cr in the $Bi_2Se_3$ samples is lower according to the XRF analysis, as summarized in Table 1. Thus, we cannot conclude on the true solubility of Cr based on this analysis. Magnetic measurements suggest the maximum solubility is $x_{MAX}$ ≤0.003 (for samples annealed at 823 K), as described below. Thus, we expect a formation of nano-precipitates, which are not detectable by powder XRD, for x≥0.003. From this perspective, the composition and properties of a sample will strongly depend on its thermal history. We use single-crystalline samples prepared from the inside of a batch since the surface might contain Cr-rich phases. Note that the theoretical XRF information depth is ≈ 12 μm thick (experimentally verified to 12–13 μm), which approaches the average bulk Cr concentration. Therefore, we use the EDX/SEM analysis as a complementary method with a much lower penetration depth, which limits the information depth. Contrary to XRF, the EDX analysis of the samples shows a lower if not zero concentration on the surface of a single crystal, independent of its composition. We performed a large number of scans to discover areas showing higher than zero concentrations, since such areas are randomly embedded throughout the crystal volume. We succeeded at the head of the BT crystal, where such precipitates form frequently due to growth from the Cr-rich melt and

occur more frequently just beneath the surface. Such a scan is depicted in Fig. 6. Expectedly, the concentration from the EDX analysis depends on the accelerating voltage U of the electron beam. While we obtain a 5 at. % Cr for U=20 kV (penetration depth of electrons ≈ 900 nm; 80% of the EDX signal is from ≈ 480 nm), the U=5 kV (penetration depth of electrons ≈ 100 nm; 80% of the EDX signal is from ≈ 55 nm) gives 16 at. % of Cr. The simulation of the penetration depth was performed with the CASINO Monte Carlo program (v2.42) [24]. This clearly indicates that the chromium forms layered inclusions within the $Bi_2Se_3$ matrix. Apparently, the perfect layered structure of the $Bi_2Se_3$ matrix is not affected by the presence of Cr (Fig. 6).

*3.2. Transport parameters*

Figs. 7, 8 and 9 present the measured temperature dependence of the electrical conductivity $\sigma$(i⊥c), the Hall coefficient $R_H$(B||c), and the Seebeck coefficient $S$(ΔT⊥c). All the samples are in a near-equilibrium state (at T=823 K) and do not change upon cycling within the measured temperature range.

The temperature dependence of the parameters suggests an extrinsic state of the semiconductor. The relationship $\mu \sim T^r$ provides insight about the scattering mechanism of free carriers [26]. To estimate the scattering mechanism, we performed a simplification and plotted $\ln(\mu_H) = \ln(R_H \cdot \sigma)$ as a function of $\ln(T)$ in Fig. 10. The exponent $r$ becomes close to -1.5 (solid line in Fig. 10) irrespective of the doping, which indicates that scattering by acoustic phonons dominates above room temperature. The behavior in the low temperature region can be explained by a mixed scattering by acoustic phonons and ionized impurities or, alternatively, by optical phonons (most pronounced for pure $Bi_2Se_3$, which possess the highest concentration of native defects, as discussed below). The room temperature values of the physical parameters are summarized in Table 1, including the actual concentration of Cr. All parameters provide evidence for the acceptor characteristics of chromium, although the actual doping efficiency remains fairly low (≈30%, providing one hole per chromium atom due to the formation of the $Cr^{+2}$ state). This indicates the formation of both $Cr_{Bi}^{-1}$ (chromium effectively in the $Cr^{+2}$ state) and $Cr_{Bi}$ (chromium effectively in the $Cr^{+3}$ state). This is in accordance with the measurement of the magnetic susceptibility, which reveals the formation of the high spin of $Cr^{+2}$.

Counter-intuitively, the mobility of the Cr-doped samples (x≤0.01) is higher than the mobility of pure $Bi_2Se_3$. This suggests some healing process leading to the increasing scattering times. We conclude that Cr reduces the amount of the two dominant defects [14]: Se vacancies $V_{Se}$ and Bi anti-sites in the place of Se, $Bi_{Se}$. In fact, the healing process could account for the acceptor-like effect in terms of the shift in the host native defect equilibrium [27]:

$$Bi_{Bi} + V_{Se}^{+2} + 2e^- \Leftrightarrow Bi_{Se}^{-1} + V_{Bi}^{-3} + 4h^+. \quad (1)$$

However, in view of the magnetic measurements, we also attribute the doping effect to the formation of the $Cr^{+2}$ state. Next to substitution, $Cr^{+2}$ can be a part of the nano-/micro-inclusions within the vdW gap. We note that the formation of the $Bi_2Cr_4Se_9$ phase keeps the stoichiometry at 2:3 for the matrix $Bi_2Se_3$.

The high-resolution XRD results in Figs. 2–4 demonstrate that the crystal quality of the Cr-doped sample is comparable to pure $Bi_2Se_3$ but still shows different features. As both samples contain randomly rotated mosaic blocks (although of a different nature), the decrease in the native point defect concentrations, rather than mosaicity, is likely to account for the enhanced mobility. An enhanced mosaicity is an inherent feature of TM-doped tetradymite crystals according to our experiments.

Note that decreasing the electron concentration should lead to an apparently enhanced effective mass and thus an apparently lower mobility, since the upper conduction band of the lower effective mass becomes completely depleted, as discussed below [26]. The same reasoning applies for S. We note that the mobility of the MBE samples is two orders of magnitude lower than the mobility in single crystals, leading to hoping like conductivity [10, 11]. However, this mobility prevents the eventual use of such samples in spintronics.

In terms of TEs, the figure of merit $Z=\sigma S^2/\kappa$ is a measure of the TE conversion efficiency of a material ($\kappa$ is thermal conductivity). Next to the low thermal conductivity, the numerator $\sigma S^2$ (so called power factor *PF*) needs to be high for a large TE performance. However, in ordinary (conventional) bulk materials, the two components σ and *S* are bound through the band structure, and an increasing $\sigma$ leads to a decreasing *S*. There are some impurities in the Bi-Sb-Te, with an extraordinary energy dependence of the density of states (DOS) leading to a large *PF*, e.g., Tl-doped PbTe [28], Sn-doped $Bi_2Te_3$ [29-31] and Ga-doped $(Bi_{0.5}Sb_{0.5})_2Te_3$ [32]. Another way of increasing the *PF* is an extraordinary scattering of the free carriers (FC). The idea can be derived from comparing the S values for the case of FC scattering on acoustic phonons and ionized impurities. The latter produces a much higher S than the former at some given Fermi levels. This is because scattering of the FC on the acoustic phonons shows much less energy dependency than scattering on the ionized impurities. In other words, the high-energy (hot) FCs are less scattered by ionized impurities than the low-energy FCs. This produces a larger S compare to the scattering on acoustic phonons. However, the scattering on ionized impurities scarcely survive room temperature due to the increasing number of phonons with the increasing temperature. Therefore, the aim is to introduce extra scattering centers (possibly charged) to provide a highly energy-dependent scattering of the FC at elevated temperatures—i.e., energy filtering of electrons. Nano-particles are one of the possible candidates [17, 18].

We observe an extraordinary behavior in Cr-doped $Bi_2Se_3$. Figure 11a shows the Seebeck coefficient as a function of the FC concentration (Pisarenko plot). The curves depict the theoretical dependence based on a simple parabolic model, which is applicable for in-plane transport parameters since the energy spectrum is almost parabolic [33]. Thus, the theoretical curves are calculated using the Fermi integrals for parabolic approximations [34]. We use the plot for T=450 K to ensure we are in the region of acoustic phonons. The picture looks similar for lower temperatures (T=300 K in Fig. 11b) and other scattering mechanisms. These curves all indicate an extraordinary behavior showing that the Seebeck coefficient does not follow the theoretical curve. The experimental slope of the function S=f(n) is higher than the theoretically predicted value, which prevents the explanation in terms of the increasing effective mass. According to [26, 33], there are two types of FCs in the conduction band: the lower conduction band of heavier electrons m=0.12 $m_0$, and the upper

conduction band with m=0.075 $m_0$, which is less populated. The two bands are separated by a very small energy ≈40 meV, which allows the parabolic approximation [26, 33]. Moreover, the Seebeck coefficient S is averaged via the electrical conductivity for the two types of FCs $S=(S_1\sigma_1+S_2\sigma_2)/(\sigma_1+\sigma_2)$ [35]. Thus, the contribution of the lower-mass electrons to the Seebeck coefficient should result in a decrease rather than an increase in S with the increasing FC concentration and vice versa (see the inset of Fig. 11a). Such results call for a comparison with other published data. As there are almost no corresponding data for T=450 K, we present the comparison with the relevant data for T=300 K in Fig. 11b. While the In-, Sb-and Fe-doped $Bi_2Se_3$ [36-38] samples obey the theoretical curve the Sr-doping [39] shows some deviations from the theoretical values, which is far weaker than those observed for the Cr-doped samples; we obtain e.g., S=87/117 $\mu VK^{-1}$ for $n\cong 0.65x10^{25}$ $m^{-3}$ for the Cr/Sr doped samples.

We believe these results could indicate the extraordinary energy filtering of free electrons. We suggest three possible mechanisms. First, Cr atoms may form defects close to conduction band edge [16] and capture an electron due to the mixed valence state $Cr^{+2}/Cr^{+3}$. Such an event can be energy selective and produce an extraordinary Seebeck coefficient. Likewise, the formation of the Cr-based nano-precipitates, as discussed above and below, can lead to the energy-dependent scattering of electrons. In that view, some planar types of defects (nano-inclusions) derived from misfit structures [16] are the real candidates. In fact, such defects may carry some charge and mimic the ionized impurity scattering at higher temperatures. Another explanation is the effect of the mosaicity feature, i.e., the formation of nano-structures due to small variations in the tilt of the trigonal axis c along single crystals in the Cr-doped crystal. Any of these processes would lead to different local charge densities and effect the energy dependence of $\mu$ and $\sigma$ [28-32]. The last explanation consists of the decrease/formation of Se vacancies and Bi anti-sites that are effective ionized scattering centers. This would suggest that the scattering from these vacancies/anti-sites survives to rather high temperature in $Bi_2Se_3$. This can be observed by comparing Figs. 11a and 11b. Namely, the presence of ionized impurity scattering at T=300 K leads to apparently higher effective masses of the electrons compared to T=450 K. Fig. 10 indicates a slight fading of the scattering from ionized impurities upon doping over the entire temperature range measured. Thus, healing of the structure can be an alternative explanation. This would also explain the decline of the Seebeck coefficient from the theoretical value. However, the *PF* should not increase when passing from ionized impurity scattering towards acoustic phonon scattering. In fact, the energy filtering is not defined a priori. Usually, the energy filtering is assumed to increase the Seebeck coefficient while the electrical conductivity decrease moderately. Here, we observe both the rising mobility (conductivity) and Seebeck coefficient (although slower than expected). This can be connected with the fact that the mobility is always higher for the scattering on paramagnetic uncharged point defects compared with any other scattering center in diluted solutions of magnetic impurities in narrow gap semiconductors [40].

There is a profound theoretical study showing that cutting off the low or high energy halves of the Fermi window can produce an enhancement or drop in the *PF* [17]. In Fig. 12, we observe an increase of the *PF*. Note that the increase is partially due to the optimization of the FC concentration [41] and partially due to the

extraordinary behavior. However, we argue that the decrease (increase) of *S* is due to neither the decreasing (increasing) degeneracy nor variation of the band effective mass, as discussed above (see also the inset of Fig. 11a). This is also evidenced by the comparison with other systems in Fig. 11b. However, the "energy filtering" should be considered as a plausible explanation rather than the only one. Clearly, this issue awaits a rigorous explanation. As another alternative, although still not explained thoroughly, we offer a remarkable discussion on effect of heavy-light band combinations (which is the case here) on TE properties of chalcopyrites in [42].

Importantly, the extraordinary behavior could be observed for samples x=0.01, 0.02 and 0.03. For these three samples, the maximum of the Seebeck coefficient *S* (and the *PF*) tends to be higher compared to pure $Bi_2Se_3$, although apparently shifted towards higher temperatures (Figs. 9 and 12). Namely, such a shift of the S-maximum towards higher temperatures is linked to an increase of the FC concentration and decrease of S in ordinary systems.

We believe this can be a rather common effect associated with the TM doping of chalcogenide materials with a small solubility of TM, as suggested in [43]. Since the nano-precipitates of varying size can better cover a larger area of the Fermi window [17-19] over monodispersed precipitates, such energy filtering can be optimized through a modification (e.g., kinetics) of the preparation route.

*3.3. Magnetic properties*

We make use of the magnetic measurements to corroborate the previous experiments and illuminate the nature of eventual precipitates. In summary, the MBE films of the Cr- doped $Bi_{2-x}Cr_xSe_3$ [10, 11] or Cr-intercalated ($Cr_xBi_2Se_3$) [12] $Bi_2Se_3$ has been studied. All papers report an unconventional FM ordering with maximum critical temperatures of 35 K for x=0.1 and 20 K for x=0.05. Contrarily, a tendency for AFM ordering has been reported for one substituted sample of a $Cr_{0.15}Bi_{1.85}Se_3$ single crystal [13]. This suggest that all forms of magnetism can appear within one single crystalline sample. The tendency towards clustering discussed above supports this conclusion in oversaturated materials. Namely, the concentration of Cr atoms can (i.e., will) vary spatially within a sample and even within a cluster. In such a case, the kinetics of sample preparation will play a major role next to thermodynamics, which otherwise would lead to equilibrium. The formation of misfit compounds reported in [16] may explain the diversity of the magnetic properties. Namely, the intralayer and interlayer interactions may produce FM and AFM ordering [16]. As a result, we find samples with various compositions within a single crystal. However, we expect to find homogeneous samples showing PM for much diluted $Bi_{2-x}Cr_xSe_3$ systems but find both AFM and FM ordering in samples that are forced to accumulate higher concentration of Cr. Indeed, the $Bi_{2-x}Cr_xSe_3$ samples with nominal x=0.005 and actual x=0.0025 show almost pure PM, indicating that chromium is truly dissolved in the matrix (Fig. 13). Even the magnetization curves show no trace of magnetic ordering. Instead, the magnetization saturates at high fields and perfectly matches the Brillouin function (Fig. 13 inset). We observe mostly the same picture for nominal x=0.01 and 0.02 (actual x=0.005 and 0.009). However, for nominal x≥0.02, the composition of the single-crystalline samples markedly varies within one batch, even for the materials prepared by FMC. Thus, two single-crystalline samples of one

batch generally show different magnetic properties and Cr contents. The analysis of the magnetic properties was as follows. First, we assume a quenching of the Cr orbital electron momentum (Cr is a *3d* element) [2]. Thus, the total momentum number *J* equals the spin momentum number *S*, *J*=*S*. We used magnetization-field data to fit the Brillouin function to obtain $J_{Brill}$ and the concentration of Cr atoms in the host matrix $n(Cr)_{Brill}$. We use the same $n(Cr)_{Brill}$ to fit the magnetization-temperature data with the Curie–Weiss (CW) law to acquire $J_{CW}$ for comparison. We used the CW law given by

$$\chi(T) = \frac{C}{T - T_{CW}} + \chi_0, \quad (2)$$

where $\chi$ is the magnetic susceptibility, *C* is the Curie constant, $T_{CW}$ is the critical paramagnetic temperature and $\chi_0$ is a temperature independent term that considers the mostly diamagnetic contributions of the host lattice. The Curie constant can be used to calculate $J_{CW}$ according to formula $C = n(Cr)g_J\mu_0\mu_B^2 J_{CW}(J_{CW}+1)$, where the Landé factor is $g_J$=2 for orbital quenching, and $\mu_0$and $\mu_B$ are the vacuum susceptibility and Bohr magneton, respectively. The parameters are summarized in Table 2.

This procedure produces a *J* that is slightly higher than the theoretical value of 1.5. This indicates the formation of both $Cr_{Bi}^{-1}$ (chromium effectively in the $Cr^{+2}$ state, *J*=2) next to $Cr_{Bi}$ (chromium effectively in the $Cr^{+3}$ state, *J*=1.5). This is in accordance with the Hall effect measurements, which reveal slight donor activity as discussed above. We assume the formation of a high spin in $Cr^{+2}$. Thus, the 4$^{th}$ unpaired electron of $Cr^{+2}$ moves to the $e_g$ orbital next to the 3 electrons in the $t_{2g}$ orbital, which is consistent with the weak-field Se matrix. Assuming the true substitutional solution (no clusters, $Cr_{Bi}$ only) of Cr in $Bi_2Se_3$ produces PM and that AFM/FM are the products of the compounds and clusters embedded in a single crystal, the maximum solubility is $x_{MAX}$ ≤0.003 (Table 2). We observe a strong inhomogeneity for the samples with a nominal x>0.02 accompanied by the formation of foreign phase of $Bi_2Cr_4Se_9$. Rather complex magnetic properties are observed for one sample $Bi_{2-x}Cr_xSe_3$ with a nominal x=0.04 (Fig. 14). While the high-temperature data CW fit gives a positive $T_{CW}$, i.e., an FM ordering, the CW fit of the low-temperature data gives a negative $T_{CW}$, i.e., an AFM ordering. Unfortunately, we observe no hysteresis in the magnetization data at any T to corroborate the FM ordering. We believe this is very soft material, i.e., the hysteresis lies within the measurement accuracy.

Such behavior can be explained by a partial occupation of the octahedral positions of the van der Waals gap by the Cr atoms. Such a partial occupation, 0.44 of the octahedral vdW positions, was described in the misfit-layer compounds from the Bi-Cr-Se system in [16]. In addition, such an accumulation of the manganese atoms in the vdW gap of the $Bi_2Te_3$ epitaxial layers was reported in [44]. According to the well-established Goodenough–Kanamori rule [e.g., 45], the exchange interaction of $Cr^{+3}$ ions (configuration $t_{2g}^3 - e_g^0$) coupled via Se atoms at 90° angle gives rise to FM ordering, which is the case for two Cr atoms in neighboring octahedral positions within the quintuple layer (QL) or vdW gap. On the other hand, the Cr-Se-Cr bridge at 180° allows the superexchange $t_{2g}^3 - t_{2g}^3$ interaction of $Cr^{+3}$ ions and is AFM in nature, which is the case for two Cr atoms within the QL or a lone Cr atom in the vdW gap coupled to Cr in place of Bi within the QL—compare the inset of Fig. 14. Thus, we have two competing interactions, FM and AFM, on the PM background of the diluted

Cr solid solution—a lone substitutional $Cr_{Bi}$ defect in the $Bi_2Se_3$ matrix (see inset in Fig. 14). We note that the mere occurrence of $Cr^{+2}$ (configuration $t_{2g}^3 - e_g^1$) facilitates FM ordering due to double exchange, i.e., due to real electron transfer among $Cr^{+3}$ and $Cr^{+2}$ ions. Interestingly, the $\chi$=f(T) is almost independent of the orientation, i.e., the results differ within measurement accuracy for in-plane and cross-plane magnetic field orientations. Such behavior is unexpected in a strongly anisotropic medium, although it is probably inherent to Cr in tetradymite crystals, as indicated by Cr-doped $Sb_2Te_3$ [2]. Strikingly, we observe the effect of the magnetic field strength (Fig. 14). Such a peculiar behavior calls for a thorough study on an even larger set of samples and is beyond the scope of this paper.

## 4. Conclusions

We prepared a series of $Bi_{2-x}Cr_xSe_3$ single crystals with a nominal x ranging between 0 and 0.04 in a near equilibrium state at T=823 K. The chromium decreases the total concentration of native defects. The true (substitutional) solubility of Cr in $Bi_2Se_3$ is x≤0.003 ($2x10^{19}$ Cr atoms per $cm^3$) at 820K. We assume the formation of nano-precipitates in the composition range (x=0.003–0.02), as the X-ray diffraction analyses indicate the presence of additional phases ($Bi_2Cr_4Se_9$) for x≥0.02. This conclusion is corroborated from the EDX/XRF analysis. The reciprocal space mapping reveals a modified mosaicity for the Cr-doped samples. We think the changes induced by the Cr doping lead to an extraordinary behavior of transport properties in $Bi_2Se_3$. The extraordinary behavior of the Seebeck coefficient and carrier mobility lead to an enhanced power factor in the doped crystals. In our view, this indicates the extraordinary energy filtering of free electrons. We suggest three possible mechanisms. First, the capture of electrons is due to the mixed valence state $Cr^{+2}/Cr^{+3}$. Further, the formation of Cr compound-based nano-precipitates leads to the energy dependent scattering of electrons. Finally, the modified mosaicity can induce a favorable energy filtering of electrons. For TE applications, further modifications of the preparation route would be beneficial in terms of optimizing the nano-structuring. A modified kinetics of the preparation may lead, for example, to a higher concentration of smaller inclusions. Furthermore, the TM induced mosaicity is expected to decrease the thermal conductivity, which is favorable for the ZT values. The magnetization data corroborates the picture drawn from the transport data. Furthermore, this indicates competing interactions of FM and AFM within the PM background of the diluted Cr solid solution in the $Bi_2Se_3$ matrix. Thus, it is worth exploring Cr-doped single crystals, especially in terms of the preparation route, as the kinetics and thermodynamics both play a role.

**Acknowledgments**

The financial support from the Grant Agency of the Czech Republic (GA CR), project No. 16-07711S is greatly appreciated. V. H. acknowledges the support by the project NanoCent financed by the European Regional

Development Fund (ERDF, project No. CZ.02.1.01/0.0/0.0/15.003/0000485). K. P. appreciates support from the grants LM2015082, ED4.100/11.0251 and CZ.02.1.01/0.0/0.0/16_013/0001829 from the Ministry of Education, Youth and Sports of the Czech Republic.

**References**

[1] G. S. Nolas, J. Sharp, H. J. Goldsmid, Thermoelectrics, Basic Principles and New Materials Developments, Springer, Berlin, Heidelberg, 2001, p. 111.
[2] J. S. Dyck, C. Drasar, P. Lostak, C. Uher, Phys. Rev. B 71 (2005) 115214.
[3] V.A. Kulbachinskii, P.M. Tarasov, E. Bruck, Physica B 368 (2005) 32–41.
[4] V. A. Kulbachinski, P. M. Tarasov, and E. Brück, JETP Letters, Vol. 81, No. 7, (2005) 342–345.
[5] V. A. Kulbachinski, P. M. Tarasov, and E. Brück, Journal of Experimental and Theoretical Physics, Vol. 101, No. 3, (2005) 528–534.
[6] Y. S. Hor, P. Roushan, H. Beidenkopf, J. Seo, D. Qu, J. G. Checkelsky, L. A. Wray, D. Hsieh, Y. Xia, S.-Y. Xu, D. Qian, M. Z. hasan, N. P. Ong, A. Yazdani, and R. J. Cava, Phys. Rev. B 81 (2010) 195203.
[7] H. Yhang, C.-X. Liu, X.-L. Qi, Y. Fang and S-C. Yhang, Nat. Phys. 5 (2009) 438.
[8] Y. L. Chen, J.G. Analytis, J.-H. Chu, Z. K. Liu, S.-K. Mo, X. L. Qi, H. J. Zhang, D. H. Lu, X. Dai, Z. Fang, S. C. Zhang, I. R. Fisher, Z. Hussain, Z.-X. Shen, Science 325 (2009) 178.
[9] K. Kuroda, M. Arita, K. Miyamoto, M. Ye, J. Jiang, A. Kimura, E. E. Krasowskii, E. V. Chulkov, H. Iwasawa, T. Okuda, K. Shimada, Y. Ueda, H. Namatame, and M. Taniguchi, Phys. Rev. Lett. 105 (2010) 076802.
[10] 7.X. F. Kou, W. J. Jiang, M. R. Lang, F. X. Xiu, L. He, Y. Wang, X. X. Yu, A. V. Fedorov, P. Zhang, and K. L. Wang, J. Appl. Phys. 112 (2012) 063912
[11] M. Liu, J. Zhang, C.-Z. Chang, Z. Zhang, X. Feng, K. Li, K. He, L.-L. Wang, X. Chen, x. Dai, Z. Fang, Q.-K. Xue, X. Ma, and Y. Wang, Phys. Rev Lett. 108 (2012) 036805
[12] P. P. J. Haazen, J.-B. Laloe, T. J. Nummy, H. J. M. Swagten, P. Jarillo-Herrero, D. Heiman, and J. S. Moodera, Appl. Phys. Lett. 100 (2012) 082404.
[13] Y. H. Choi, N. H. Jo, K. J. Lee, J. B. Yoon, C. Y. You, and M. H. Jung, J. Appl. Phys. 109 (2011) 07E312 .
[14] J.-M. Zhang, W. Ming, Z. Huang, G.-B. Liu, X. Kou, Y. Fan, K. L. Wang, and Y. Yao, Phys. Rev. B 88 (2013) 235131.
[15] G. G. Shabunina, E. V. Kireeva, T. G. Aminov, Russ. J. Inorg. Chem. 41 (1996) 1496.
[16] S. M. Clarke and D. E. Feedman, Inorg. Chem. 54 (2015) 2765.
[17] J.-H. Bahk, Z. Bian, M. Zebarjadi, P. Santhanam, R. Ram, Appl. Phys. Lett. 99 (2011) 072118.
[18] S. V. Faleev,and F. Leonard, Phys. Rev. B 77 (2008) 214304.
[19] D. Narducci, E. Selezneva, G. Cerofoliny, S. Frabboni, G. Ottaviani, J. Solid State Chem. 193 (2012) 19.
[20] R. D. Shannon, Acta Crystallographica A32 (1976) 751.
[21] S. Nakajima, J. Phys. Chem. Solids 24 (1963) 479.
[22] U. Pietsch, V. Holy and T. Baumbach, *High-Resolution X-Ray Scattering From Thin Films to Lateral Nanostructures* (Springer-Verlag, Berlin, Heidelberg, New York 2004).
[23] H. Steiner, V. Volobuev, O. Caha, G. Bauer, G. Springholz and V. Holy, J. Appl. Cryst. 47 (2014) 1889.
[24] Drouin, D., Couture, A. R., Joly, D., Tastet, X., Aimez, V. and Gauvin, R. (2007). Scanning 29 (2007) 92.
[25] M. Balkanski R. F. Wallis, Semiconductor Physics and Applications, Oxford University Press, Oxford, 2000, p. 190-191.
[26] V. A. Kulbachinskii, N. Miura, H. Nakagawa, H. Arimoto, T. Ikaida, P. Lostak, C. Drasar, Phys. Rev. B 59 (1999) 15733.
[27] P. Ruleova, C. Drasar, A. Krejcova, L. Benes, J. Horak, P. Lostak, J. Phys. Chem. Solids 74 (2013) 746.
[28] J. P. Heremans, V. Jovovic, E. S. Toberer, A. Saramat, K. Kurosaki, A. Charoenphakdee, S. Yamanaka, G. J. Snyder, Science 321 (2008) 554.
[29] V.A. Kulbachinskii, N.B. Brandt, P.A. Cheremnykh, S.A. Azou, J . Horak, and P. Lostak, phys. stat. sol. (b) 160 (1988) 237-243.

[30] V. A. Kulbachinskii, H. Negishi, M. Sasaki, Y. Giman, M. Inoue, P. Lostak, and J. Horak, phys. stat. sol. (b) 199 (1997) 505-513.
[31] C.M. Jaworski, V. Kulbachinskii, J.P. Heremans, Phys. Rev. B 80 (2009) 233201.
[32] V. A. Kulbachinskii, V. G. Kytin, P. M. Tarasov, and N. A. Yuzeeva, Physics of the Solid State, Vol. 52, No. 9, (2010) 1830–1835.
[33] V. A. Kulbachinskii, N. Miura, H. Arimoto, T. Ikaida, P. Lostak, J. Horak, and C. Drasar, J. Phys. Soc. Japan 68 (1999) 3328.
[34] N. Cheng, R. Liu, S. Bai, X. I. Chen, J. Appl. Phys. 115 (2014) 163705.
[35] C. M. Bhandari, D. M. Rowe, in CRC Handbook of Thermoelectrics, ed. by D. M. Rowe (CRC Press, New York, 1994) p. 49.
[36] P. Lostak, L. Benes, S. Civis, H. Sussmann, J. Mater. Sci. 25 (1990) 277.
[37] P. Lostak, C. Drasar, I. Klichova, J. Navratil, T. Cernohorsky, Phys Status Solidi B 200 (1997) 289.
[38] V. A. Kulbachinskii, N. Miura, H. Nakagawa, H. Arimoto, T. Ikaida, P. Lostak, and C. Drasar, Phys. Rev. B, 59 (1999) 15733.
[39] P. Ruleova, C. Drasar, A. Krejcova, L. Benes, J. Horak, P. Lostak, J. Phys. Chem. Solids 74 (2013) 746.
[40] J. Kossut, phys. stat. sol.(b) 72 (1975) 359.
[41] G. Min, J. Electron. Mater. 39 (2010) 2459.
[42] D. Parker and D. Singh, Phys. Rev. B 85 (2012) 125209.
[43] J. Friedel, Can.J.Phys. 34 (1956) 1190.
[44] J. Ruzicka, O. Caha, V. Holy, H. Steiner, V. Volobuiev, A. Ney, G. Bauer, T. Duchon, K. Veltruska, I. Khalakhan, V. Matolin, E. F. Schwier, H. Iwasawa, K. Shimada and G. Springholz, New J. Phys. 17 (2015) 013028.
[45] J. S. Zhou and J. B. Goodenough, Phys. Rev. Lett. 96 (2006) 247202.

**Figures**

Fig. 1. XRD patterns of $Bi_{2-x}Cr_xSe_3$ single crystals for nominal x=0-0.04. There is clear evidence of an additional phase (peak at 2Θ = 31.3°) for x=0.03 and 0.04, which can be attributed to either $BiCrSe_3$ or $Bi_2Cr_4Se_9$. This peak is barely detectable for nominal x=0.02. The patterns are shifted vertically for clarity.

Fig. 2. Symmetric HR XRD scan of the $Bi_2Se_3$ and $Bi_{1.99}Cr_{0.01}Se_3$ single crystals (points) and the simulated curve (lines) using the crystallographic data of pure $Bi_2Se_3$ from [18]. The vertical lines denote the positions of the diffraction maxima 000L, the curves of the Cr-doped sample are shifted vertically for clarity.

Fig. 3. High-resolution XRD reciprocal-space maps measured around the 000.15 reciprocal-lattice points of the single crystals $Bi_{1.99}Cr_{0.01}Se_3$ (top panel) and $Bi_2Se_3$ (bottom). The color scale covers four decades of scattered intensity.

Fig. 4. The linear scans extracted from the reciprocal-space maps in Fig. 3 along the horizontal (a) and vertical directions (b). The arrows denote the features discussed in the text.

Fig. 5. XRF mapping of chromium (top) in the $Bi_2Cr_{0.01}Se_3$ BT grown single crystals (bottom; black rectangle corresponds to the analyzed area). The strong inhomogeneity in the Cr distribution is evident. Note that the Cr concentration increases towards the Bridgman crystal end (head), which indicates that the solubility of Cr is higher in the liquid phase than in the solid phase.

Fig. 6. The SEM/EDX mapping of chromium in $Bi_{2-x}Cr_xSe_3$ BT-grown single crystals.

Fig. 7. Electrical conductivity as a function of temperature for the $Bi_{2-x}Cr_xSe_3$ single crystals.

Fig. 8. Hall coefficient as a function of temperature for the $Bi_{2-x}Cr_xSe_3$ single crystals. The concentration of electrons n can be calculated using the following formula: $n=r_H/R_He$. The Hall factor $r_H$ is a constant for one particular temperature. Note that the very small difference in the effective mass (and thus mobility) of electrons in the two electron bands (discussed below) guaranties one can use this simple formula. Although

one would obtain $r_H \cong 0.8$ for acoustic phonons [25], we use $r_H=1$ to maintain the correspondence with the literature [e.g.26].

Fig. 9. Seebeck coefficient as a function of temperature for the $Bi_{2-x}Cr_xSe_3$ single crystals.

Fig. 10. Hall mobility as a function of temperature in a natural log-scale for the $Bi_{2-x}Cr_xSe_3$ single crystals. The solid line corresponds to scattering of acoustic phonons. Note that the scattering of acoustic phonons dominates above T=400 K, irrespective of the doping.

Fig. 11. a) Seebeck coefficient as a function of the Hall carrier concentration for $r_H=1$ (Pisarenko plot) for the $Bi_{2-x}Cr_xSe_3$ single crystals at T=450 K. Note that using $r_H=0.8$ (note at caption of Fig. 8) would shift the points towards lower carrier concentrations, but would not change the slope. The $\tau$ denotes samples annealed at920 K. Inset documents the depletion of the light electron (le) band upon decrease of the electron concentration. The heavy electron (he) band populated implies a rather higher Seebeck coefficient than predicted by the Pisarenko plot. This contradicts the experiment. b) The comparison of $Bi_{2-x}Cr_xSe_3$ with the $Bi_2Se_3$ single crystals doped with other elements showing the extraordinary behavior of Cr in the $Bi_2Se_3$ matrix. We quote the references in Section 3.2.

Fig. 12. Power factor as a function of temperature for the $Bi_{2-x}Cr_xSe_3$ single crystals.

Fig. 13. Susceptibility as a function of temperature for the $Bi_{2-x}Cr_xSe_3$ single crystal with a nominal x=0.005. The solid curve is a fit to the Curie–Weiss law. Inset: Magnetization as a function the magnetic field strength for the $Bi_{2-x}Cr_xSe_3$ single crystal with a nominal x=0.005. The solid curve represents the fit to the Brillouin function. The diamagnetic part proportional to field B was subtracted from the experimental values.

Fig. 14. Susceptibility as a function of temperature for the $Bi_{1.96}Cr_{0.04}Se_3$ single crystal for B=1 and 7 T. The solid lines are the fits according to the CW law. The outputs are summarized in Table 2. Inset: Three ways of embedding a small number of Cr atoms within the quintuple layers (QL) or between QL—in the vdW gap of $Bi_2Se_3$ leading to PM, FM, and AFM state—please compare with text.

# Thermoelectric and magnetic properties of Cr-doped single crystal $Bi_2Se_3$ – search for energy filtering.

P. Cermak[1], P. Ruleova[1], V. Holy[2,3], J. Prokleska[2], V. Kucek[1], K. Palka[1,4], L. Benes[1], C. Drasar[5*]

[1]*Department of General and Inorganic Chemistry, Faculty of Chemical Technology, University of Pardubice, Studentska 573, 532 10 Pardubice, Czech Republic*

[2]*Department of Condensed Matter Physics, Faculty of Mathematics and Physics, Charles University, Ke Karlovu 3, 121 16 Praha 2, Czech Republic*

[3]*Masaryk University, Department of Condensed Matter Physics and CEITEC, Kotlářská 2, 61137 Brno, Czech Republic*

[4]*Center of Materials and Nanotechnologies - CEMNAT, Faculty of Chemical Technology, University of Pardubice, nam. Cs. legii 565, 530 02 Pardubice, Czech Republic*

[5]*Institute of Applied Physics and Mathematics, Faculty of Chemical Technology, University of Pardubice, Studentska 573, 532 10 Pardubice, Czech Republic*

[*]corresponding author: cestmir.drasar@upce.cz, phone: ±420466036036

**Abstract**

Thermoelectric effects are one of the promising ways to utilize waste heat. Novel approaches have appeared in recent decades aiming to enhance thermoelectric conversion. The theory of energy filtering of free carriers by inclusions ranks is among the latest developed methods. Although the basic idea is clear, experimental evidence of this phenomenon is rare. Based on this concept, we searched suitable systems with stable structures showing energy filtering. Here, we report on the anomalous behavior of Cr-doped single-crystal $Bi_2Se_3$ that indicates energy filtering. The solubility of chromium in $Bi_2Se_3$ was studied, which is the key parameter in the formation process of inclusions. We present recent results on the effect of Cr-doping on the transport coefficients on a wide set of single crystalline samples. Magnetic measurements were used to corroborate the conclusions drawn from the transport and X-ray measurements.

**Key words**

Thermoelectrics; single crystal; transition metal doping; energy filtering; tetradymite

## 1. Introduction

$Bi_2Se_3$, which adopts the tetradymite structure, is one of the constituents of room-temperature thermoelectric (TE) materials [1]. Some of these tetradymite materials have been shown to form diluted magnetic semiconductors (DMS) if they are doped with certain transition metals (TM). A variety of magnetic

ordering has been reported, although the interactions leading to the ordering is still subject to discussion [2-6]. The reason is that there are most likely two or more types of interactions in each TM doped sample. The discovery that these materials are 3D topological insulators (TI) [7-9] has led to renewed attention to doping these materials with magnetic impurities. Among many other materials, $Bi_2Se_3$ is the most promising for electronic applications since its surface states consist of a single Dirac cone, and the material has a reasonably large band gap to guarantee an eventually very low bulk electrical conductivity. The common point to all the works is the spin manipulation. The Ferromagnetism (FM) in Cr-doped [10, 11] or Cr-intercalated [12] $Bi_2Se_3$ has been reported for MBE thin films. Contrarily, an antiferromagnetic (AFM) ordering has been reported for one sample of a Cr-doped $Bi_2Se_3$ single crystal [13]. All reports differ in properties and solubility for the magnetic impurity, and the authors admit that an interaction leading to a magnetic ordering is still unclear and call for further studies. There are profound theoretical calculations reported on the energy formation of defects [e.g., 14], which are very helpful as a guide in terms of tendencies along the periodic table (e.g., V, Cr, Mn, and Fe). Although ref. [14] suggests a slightly negative formation energy of Cr point defects in place of Bi, $Cr_{Bi}$, (i.e., spontaneous formation of such defects), we found the actual concentration of Cr is always lower than the nominal one in our single crystals, which indicates the opposite. Moreover, we found a tendency of clustering when the single crystals are forced to incorporate higher concentrations of Cr during growth from a Cr-rich melt e.g., in Bridgman crystal; Fig. 5 (below) shows an XRF mapping of Cr close to the end (head) of the Bridgman single crystal for x =0.01. In addition, other phases ($Bi_2Cr_4Se_9$) appear for x≥0.02 in the XRD patterns of our single crystals. This is in accordance with the phase diagram indicating the solubility of Cr in the solid $Bi_2Se_3$ is close to zero, while the liquid state $Bi_2Se_3$ dissolves up to 20% of $Cr_2Se_3$ at 1170 K [15]. Two incongruent compounds are formed in the pseudo-binary phase diagram: the daltonide $Bi_2Cr_4Se_9$, and the berthollide with an approximate composition of $Bi_5Cr_4Se_{13}$. An extraordinary paramagnetism is reported in Bi-Cr-Se ternary misfit-layer compounds based on these two compounds [16].

Following these results, we aim to prepare single-crystal $Bi_{2-x}Cr_xSe_3$ as close to equilibrium as possible for a given temperature to provide a detailed comparison for theoretical and experimental works. The motivation is to provide more insight into the TM-doped tetradymites. There are many uncertainties, including that the equilibrium solubility is lower than that expected from the theoretical predictions. Contrary to some papers [10-13], our results suggest that both AFM and FM ordering exist next to paramagnetism (PM) in this material. Notably, we show that doping with TM might be interesting in terms of TE applications. Namely, TMs are candidates for extra energy filtering of free carriers, which is a way to increase the efficiency of TE materials [17-19]. We think that nano-structuring may explain the extraordinary behavior. We are aware that many questions are not satisfactorily answered, but we hope they can serve as an inspiration.

## 2. Experiment

Single crystals of $Bi_{2-x}Cr_xSe_3$, with nominal x values between 0 and 0.04, were grown by heating stoichiometric mixtures of 5N Bi, Se and $Cr_2Se_3$. The synthesis of $Cr_2Se_3$ was carried out by heating stoichiometric mixtures of 5N purity elements at 1300 K for 7 days in quartz ampoules (all from Sigma-Aldrich).

The crystal growth process involved cooling from 1073 K to 923 K at a rate of 6 K per hour. The crystals were then annealed for 500 hours at 823 K in the same ampoule and then quenched in air. This free melt crystallization (FMC) produces single crystals that are 10–20 mm in length, 3–6 mm wide and up to 3 mm thick. In addition, $Bi_{2-x}Cr_xSe_3$ single crystals were grown using the Bridgman technique (BT) to better understand the behavior of Cr during growth. Contrary to FMC, the BT shows a directional crystallization par excellence. Thus, the liquidus–solidus distribution coefficient of the dopant in the $Bi_2Se_3$ plays an important role. Mostly, the solubility of the doping TM is higher in the liquid phase, as is in case of Cr, and the liquid phase becomes richer in Cr along the direction of crystal growth. Thus, the concentration of chromium increases along the single crystals up to the highest solubility, after which precipitates are eventually formed at a given temperature. The BT produces single crystals up to 60 mm in length, 8 mm wide and 5 mm thick. The orientation of all single crystals was determined using the single-crystal X-ray technique. For the physical property measurements, the FMC specimens with dimensions of 10-15 x 3 x (0.1–0.2) $mm^3$ were cut from the single crystals. The actual doping level and macroscopic homogeneity was examined using XRF mapping with a μ-XRF spectrometer M4 TORNADO (Bruker), Rh-50keV, equipped with polycapillary X-ray optics. To reveal the microscopic homogeneity, we employed energy dispersive X-ray microanalysis (EDX) using scanning electron microscopy (SEM) LYRA 3 (Tescan) equipped with an EDX analyzer Aztec X-Max 20 (Oxford Instruments).

The diffraction patterns (Cu Kα, λ = 1.5418 Å) were recorded on powdered samples using a D8 Advance diffractometer (Bruker AXS, Germany) with a Bragg–Brentano Θ-Θ goniometer (radius 217.5 mm) equipped with a Ni-beta filter and a LynxEye detector. The scan was performed at room temperature from 10 to 90° (2Θ) in 0.01° steps with a counting time of 2 s per step. The lattice parameters were refined using the Le Bail method as implemented in the program FullProf.

High-resolution X-ray diffraction (HR XRD) on single-crystalline $Bi_{2-x}Cr_xSe_3$ samples was carried out on a PaNalytical Expert-Pro diffractometer, equipped with a sealed CuKα tube, primary parabolic multilayer optics, a 2x220Ge single-crystal monochromator, a 3x220Ge analyzer, and a proportional point detector. Using this high-resolution setup, we were able to measure the reciprocal-space distribution of the diffracted intensity with a resolution down to $10^{-4}$ $Å^{-1}$.

The transport parameters include the electrical conductivity $\sigma(i\perp c)$, the Hall coefficient $R_H(B||c)$, and the Seebeck coefficient $S(\Delta T\perp c)$. These parameters were measured in the direction perpendicular to the trigonal axis, *c*, i.e., the electric field and thermal gradients were applied in the basal plane while the magnetic induction vector was parallel to the *c* axis. All parameters were measured over a temperature range from 80 K to 470 K, and a conductive graphite adhesive was used to attach the current leads. Platinum wires (50 μm in diameter) were attached along the sample using thermocompression to measure the voltage drop. The Hall effect and electrical conductivity were examined using a lock-in nano-voltmeter with a 29-Hz excitation and a static magnetic field of 0.6 T. The Seebeck coefficient was determined using the longitudinal steady-state technique with a temperature difference ranging from 3 to 3.5 K. The thermal gradients were measured with

the aid of fine copper-constantan thermocouples. The magnetic properties were investigated using an MPMS apparatus (Quantum Design).

## 3. Results and Discussion

### *3.1. X-ray analysis, XRF analysis, SEM*

A typical X-ray diffraction pattern of $Bi_{2-x}Cr_xSe_3$ obtained for powdered single crystals is shown in Fig. 1. Although all the diffraction peaks can be attributed to the structure of the $Bi_2Se_3$ for x≤0.01, there is clear evidence of additional phases (one peak at 2Θ = 31.3° attributable to both the $Bi_2Cr_4Se_9$ and γ-phase (approximate composition $BiCrSe_3$)) at x=0.03 and x=0.04. This peak is barely detectable for a nominal composition $Bi_{1.98}Cr_{0.02}Se_3$, even for very fine measurements. Thus, the equilibrium solubility of Cr in $Bi_2Se_3$ at 820 K lies below x=0.02. For the TE, this is the nominal concentration over which the micro-precipitates (X-ray detectable) of other phases might form. Thus, the nano-precipitates might form at far lower Cr concentrations depending on the growth kinetics. The lattice parameters of the parent material, $a$ = 0.41387 nm and $c$ = 2.86303 nm, are in good agreement with those in the database (PDF-4+/ICDD). We observe that the lattice parameters decrease moderately with the increase of the Cr concentration. Table 1 summarizes the lattice parameter values of $a$ and $c$ for $Bi_{2-x}Cr_xSe_3$. Note that although the actual concentrations of the dopant are small, the crystal radii of the substitutional Cr ($r(Cr^{+3})$ = 0.0755 nm and $r(Cr^{+2})$ = 0.094 nm) are much smaller than that of Bi ($r(Bi^{+3})$ = 0.117 nm) [20]. The slight but measurable drop from doping is close to the experimental errors according to our measurements. Thus, we can observe some solubility of Cr in $Bi_2Se_3$, but we are not able to discuss the solubility of Cr within Vegard´s law.

Figs. 2–4 show the results of the HR XRD diffraction experiments. In Fig. 2, we plotted the symmetric 2theta/omega scan measured on the $Bi_2Se_3$ and $Bi_{2-x}Cr_xSe_3$ (x=0.01) single crystals (points) along with the simulations (lines). Since the sample surface was (0001), the scan trajectory in the reciprocal space crosses the reciprocal-lattice points 000*L*; however, only the diffraction maxima *L*=3,6,… are allowed. The theoretical positions of the maxima are denoted by the vertical dotted lines.

The curves were simulated using the crystallographic data from ref. [21]. The comparison of the measured and simulated curves reveals the excellent quality of the investigated sample; there are neither traces of diffuse scattering from Cr-rich precipitates nor extra peaks from other $Bi_mSe_n$ phases. However, the sensitivity of the HR XRD to the presence of foreign phases is much weaker than that of the powder XRD. The amplitudes of the measured and simulated diffraction maxima 000*L* differ more for the $Bi_{1.99}Cr_{0.01}Se_3$ sample than for the $Bi_2Se_3$. This can be ascribed to the fact that the distances of the basal (0001) planes in the Cr-doped sample differ from the tabulated values, which might be caused by the Cr atoms in the lattice positions and in the vdW gap.

Since the scattering vector in this scan is always perpendicular to the sample surface, this type of scan cannot detect randomly rotated mosaic blocks. To visualize this type of defect, we measured the reciprocal-space maps around the main maximum 000.15 (see [22, 23] for more details) of the $Bi_{1.99}Cr_{0.01}Se_3$ sample and

of a pure $Bi_2Se_3$ single crystal (Fig. 3). Fig. 4(a,b) shows the linear scans extracted from the measured maps along the $Q_x$ and $Q_z$ axes, respectively. The reciprocal-space maps demonstrate the good crystal quality. The horizontal diffuse elongation of the diffraction maxima can be observed in both the $Bi_{1.99}Cr_{0.01}Se_3$ and $Bi_2Se_3$ samples, which is caused by randomly rotated mosaic blocks. Nevertheless, in both investigated samples, the main maximum is approximately 100 times higher than the diffuse peak. From this fact, we conclude that the majority of the sample volume is not rotated, and the rotated blocks make up less than approximately 1 percent of the total irradiated volume. Detailed inspection of the data reveals two interesting features that are visible mainly in the $Q_x$-scans from Fig. 4(a). The curve of sample $Bi_{1.99}Cr_{0.01}Se_3$ always contains a rather sharp side maximum (blue arrow in Fig. 4(a)). This maximum most likely stems from a misoriented large mosaic block. The degree of the block misorientation can be estimated as 0.26° with respect to the surrounding crystal matrix, and its lateral size can be compared to the coherence width of the primary X-ray beam, i.e., 0.5–1.0 μm. A similar feature can be found on the $Q_x$-scan of $Bi_2Se_3$ [red arrow in Fig. 4(b)]. The interpretation of this effect is complicated and might be caused by many misoriented blocks (misorientation on the order of 1 deg). Thus, the blocks are probably very small in the lateral direction (tens of nm). Fig. 4(b) shows the vertical ($Q_z$-) scans extracted from Fig. 3. The $Q_z$-scans of both samples are very similar, and their widths are comparable to the experimental resolution. This finding indicates that the distances of the (0001) basal planes in the rotated mosaic blocks and in the main crystal are the same, i.e., the local lattices of the blocks are only rotated and not strained. The physical nature of these blocks is not clear. For example, they can be created by laterally small faults in the stacking of the Bi-Se basal atomic planes (stacking faults or twins). The effect of the dislocations is less likely, since no deformation of the block lattices was observed.

Fig. 5 shows the XRF mapping (≈ 100 μm mean penetration depth) of the cleaving plane of the BT single crystals. In fact, we observed random cluster formation in all studied single crystals for x≥0.01, although the occurrence decreases markedly with the drop of the Cr content. Furthermore, the increasing concentration of Cr is apparent towards the end of the BT crystal, which indicates a higher solubility of Cr in liquid rather than the solid phase. In fact, the actual solubility of Cr in the $Bi_2Se_3$ samples is lower according to the XRF analysis, as summarized in Table 1. Thus, we cannot conclude on the true solubility of Cr based on this analysis. Magnetic measurements suggest the maximum solubility is $x_{MAX}$ ≤0.003 (for samples annealed at 823 K), as described below. Thus, we expect a formation of nano-precipitates, which are not detectable by powder XRD, for x≥0.003. From this perspective, the composition and properties of a sample will strongly depend on its thermal history. We use single-crystalline samples prepared from the inside of a batch since the surface might contain Cr-rich phases. Note that the theoretical XRF information depth is ≈ 12 μm thick (experimentally verified to 12–13 μm), which approaches the average bulk Cr concentration. Therefore, we use the EDX/SEM analysis as a complementary method with a much lower penetration depth, which limits the information depth. Contrary to XRF, the EDX analysis of the samples shows a lower if not zero concentration on the surface of a single crystal, independent of its composition. We performed a large number of scans to discover areas showing higher than zero concentrations, since such areas are randomly embedded throughout the crystal volume. We succeeded at the head of the BT crystal, where such precipitates form frequently due to growth from the Cr-rich melt and

occur more frequently just beneath the surface. Such a scan is depicted in Fig. 6. Expectedly, the concentration from the EDX analysis depends on the accelerating voltage U of the electron beam. While we obtain a 5 at. % Cr for U=20 kV (penetration depth of electrons ≈ 900 nm; 80% of the EDX signal is from ≈ 480 nm), the U=5 kV (penetration depth of electrons ≈ 100 nm; 80% of the EDX signal is from ≈ 55 nm) gives 16 at. % of Cr. The simulation of the penetration depth was performed with the CASINO Monte Carlo program (v2.42) [24]. This clearly indicates that the chromium forms layered inclusions within the $Bi_2Se_3$ matrix. Apparently, the perfect layered structure of the $Bi_2Se_3$ matrix is not affected by the presence of Cr (Fig. 6).

*3.2. Transport parameters*

Figs. 7, 8 and 9 present the measured temperature dependence of the electrical conductivity $\sigma$(i⊥c), the Hall coefficient $R_H$(B||c), and the Seebeck coefficient $S$(ΔT⊥c). All the samples are in a near-equilibrium state (at T=823 K) and do not change upon cycling within the measured temperature range.

The temperature dependence of the parameters suggests an extrinsic state of the semiconductor. The relationship $\mu \sim T^r$ provides insight about the scattering mechanism of free carriers [26]. To estimate the scattering mechanism, we performed a simplification and plotted $\ln(\mu_H) = \ln(R_H \cdot \sigma)$ as a function of $\ln(T)$ in Fig. 10. The exponent $r$ becomes close to -1.5 (solid line in Fig. 10) irrespective of the doping, which indicates that scattering by acoustic phonons dominates above room temperature. The behavior in the low temperature region can be explained by a mixed scattering by acoustic phonons and ionized impurities or, alternatively, by optical phonons (most pronounced for pure $Bi_2Se_3$, which possess the highest concentration of native defects, as discussed below). The room temperature values of the physical parameters are summarized in Table 1, including the actual concentration of Cr. All parameters provide evidence for the acceptor characteristics of chromium, although the actual doping efficiency remains fairly low (≈30%, providing one hole per chromium atom due to the formation of the $Cr^{+2}$ state). This indicates the formation of both $Cr_{Bi}^{-1}$ (chromium effectively in the $Cr^{+2}$ state) and $Cr_{Bi}$ (chromium effectively in the $Cr^{+3}$ state). This is in accordance with the measurement of the magnetic susceptibility, which reveals the formation of the high spin of $Cr^{+2}$.

Counter-intuitively, the mobility of the Cr-doped samples (x≤0.01) is higher than the mobility of pure $Bi_2Se_3$. This suggests some healing process leading to the increasing scattering times. We conclude that Cr reduces the amount of the two dominant defects [14]: Se vacancies $V_{Se}$ and Bi anti-sites in the place of Se, $Bi_{Se}$. In fact, the healing process could account for the acceptor-like effect in terms of the shift in the host native defect equilibrium [27]:

$$Bi_{Bi} + V_{Se}^{+2} + 2e^- \Leftrightarrow Bi_{Se}^{-1} + V_{Bi}^{-3} + 4h^+. \quad (1)$$

However, in view of the magnetic measurements, we also attribute the doping effect to the formation of the $Cr^{+2}$ state. Next to substitution, $Cr^{+2}$ can be a part of the nano-/micro-inclusions within the vdW gap. We note that the formation of the $Bi_2Cr_4Se_9$ phase keeps the stoichiometry at 2:3 for the matrix $Bi_2Se_3$.

The high-resolution XRD results in Figs. 2–4 demonstrate that the crystal quality of the Cr-doped sample is comparable to pure $Bi_2Se_3$ but still shows different features. As both samples contain randomly rotated mosaic blocks (although of a different nature), the decrease in the native point defect concentrations, rather than mosaicity, is likely to account for the enhanced mobility. An enhanced mosaicity is an inherent feature of TM-doped tetradymite crystals according to our experiments.

Note that decreasing the electron concentration should lead to an apparently enhanced effective mass and thus an apparently lower mobility, since the upper conduction band of the lower effective mass becomes completely depleted, as discussed below [26]. The same reasoning applies for S. We note that the mobility of the MBE samples is two orders of magnitude lower than the mobility in single crystals, leading to hoping like conductivity [10, 11]. However, this mobility prevents the eventual use of such samples in spintronics.

In terms of TEs, the figure of merit $Z=\sigma S^2/\kappa$ is a measure of the TE conversion efficiency of a material ($\kappa$ is thermal conductivity). Next to the low thermal conductivity, the numerator $\sigma S^2$ (so called power factor *PF*) needs to be high for a large TE performance. However, in ordinary (conventional) bulk materials, the two components σ and *S* are bound through the band structure, and an increasing $\sigma$ leads to a decreasing *S*. There are some impurities in the Bi-Sb-Te, with an extraordinary energy dependence of the density of states (DOS) leading to a large *PF*, e.g., Tl-doped PbTe [28], Sn-doped $Bi_2Te_3$ [29-31] and Ga-doped $(Bi_{0.5}Sb_{0.5})_2Te_3$ [32]. Another way of increasing the *PF* is an extraordinary scattering of the free carriers (FC). The idea can be derived from comparing the S values for the case of FC scattering on acoustic phonons and ionized impurities. The latter produces a much higher S than the former at some given Fermi levels. This is because scattering of the FC on the acoustic phonons shows much less energy dependency than scattering on the ionized impurities. In other words, the high-energy (hot) FCs are less scattered by ionized impurities than the low-energy FCs. This produces a larger S compare to the scattering on acoustic phonons. However, the scattering on ionized impurities scarcely survive room temperature due to the increasing number of phonons with the increasing temperature. Therefore, the aim is to introduce extra scattering centers (possibly charged) to provide a highly energy-dependent scattering of the FC at elevated temperatures—i.e., energy filtering of electrons. Nano-particles are one of the possible candidates [17, 18].

We observe an extraordinary behavior in Cr-doped $Bi_2Se_3$. Figure 11a shows the Seebeck coefficient as a function of the FC concentration (Pisarenko plot). The curves depict the theoretical dependence based on a simple parabolic model, which is applicable for in-plane transport parameters since the energy spectrum is almost parabolic [33]. Thus, the theoretical curves are calculated using the Fermi integrals for parabolic approximations [34]. We use the plot for T=450 K to ensure we are in the region of acoustic phonons. The picture looks similar for lower temperatures (T=300 K in Fig. 11b) and other scattering mechanisms. These curves all indicate an extraordinary behavior showing that the Seebeck coefficient does not follow the theoretical curve. The experimental slope of the function S=f(n) is higher than the theoretically predicted value, which prevents the explanation in terms of the increasing effective mass. According to [26, 33], there are two types of FCs in the conduction band: the lower conduction band of heavier electrons m=0.12 $m_0$, and the upper

conduction band with m=0.075 $m_0$, which is less populated. The two bands are separated by a very small energy ≈40 meV, which allows the parabolic approximation [26, 33]. Moreover, the Seebeck coefficient S is averaged via the electrical conductivity for the two types of FCs $S=(S_1\sigma_1+S_2\sigma_2)/(\sigma_1+\sigma_2)$ [35]. Thus, the contribution of the lower-mass electrons to the Seebeck coefficient should result in a decrease rather than an increase in S with the increasing FC concentration and vice versa (see the inset of Fig. 11a). Such results call for a comparison with other published data. As there are almost no corresponding data for T=450 K, we present the comparison with the relevant data for T=300 K in Fig. 11b. While the In-, Sb-and Fe-doped $Bi_2Se_3$ [36-38] samples obey the theoretical curve the Sr-doping [39] shows some deviations from the theoretical values, which is far weaker than those observed for the Cr-doped samples; we obtain e.g., $S=87/117\ \mu VK^{-1}$ for $n\cong0.65x10^{25}\ m^{-3}$ for the Cr/Sr doped samples.

We believe these results could indicate the extraordinary energy filtering of free electrons. We suggest three possible mechanisms. First, Cr atoms may form defects close to conduction band edge [16] and capture an electron due to the mixed valence state $Cr^{+2}/Cr^{+3}$. Such an event can be energy selective and produce an extraordinary Seebeck coefficient. Likewise, the formation of the Cr-based nano-precipitates, as discussed above and below, can lead to the energy-dependent scattering of electrons. In that view, some planar types of defects (nano-inclusions) derived from misfit structures [16] are the real candidates. In fact, such defects may carry some charge and mimic the ionized impurity scattering at higher temperatures. Another explanation is the effect of the mosaicity feature, i.e., the formation of nano-structures due to small variations in the tilt of the trigonal axis c along single crystals in the Cr-doped crystal. Any of these processes would lead to different local charge densities and effect the energy dependence of $\mu$ and $\sigma$ [28-32]. The last explanation consists of the decrease/formation of Se vacancies and Bi anti-sites that are effective ionized scattering centers. This would suggest that the scattering from these vacancies/anti-sites survives to rather high temperature in $Bi_2Se_3$. This can be observed by comparing Figs. 11a and 11b. Namely, the presence of ionized impurity scattering at T=300 K leads to apparently higher effective masses of the electrons compared to T=450 K. Fig. 10 indicates a slight fading of the scattering from ionized impurities upon doping over the entire temperature range measured. Thus, healing of the structure can be an alternative explanation. This would also explain the decline of the Seebeck coefficient from the theoretical value. However, the *PF* should not increase when passing from ionized impurity scattering towards acoustic phonon scattering. In fact, the energy filtering is not defined a priori. Usually, the energy filtering is assumed to increase the Seebeck coefficient while the electrical conductivity decrease moderately. Here, we observe both the rising mobility (conductivity) and Seebeck coefficient (although slower than expected). This can be connected with the fact that the mobility is always higher for the scattering on paramagnetic uncharged point defects compared with any other scattering center in diluted solutions of magnetic impurities in narrow gap semiconductors [40].

There is a profound theoretical study showing that cutting off the low or high energy halves of the Fermi window can produce an enhancement or drop in the *PF* [17]. In Fig. 12, we observe an increase of the *PF*. Note that the increase is partially due to the optimization of the FC concentration [41] and partially due to the

extraordinary behavior. However, we argue that the decrease (increase) of *S* is due to neither the decreasing (increasing) degeneracy nor variation of the band effective mass, as discussed above (see also the inset of Fig. 11a). This is also evidenced by the comparison with other systems in Fig. 11b. However, the "energy filtering" should be considered as a plausible explanation rather than the only one. Clearly, this issue awaits a rigorous explanation. As another alternative, although still not explained thoroughly, we offer a remarkable discussion on effect of heavy-light band combinations (which is the case here) on TE properties of chalcopyrites in [42].

Importantly, the extraordinary behavior could be observed for samples x=0.01, 0.02 and 0.03. For these three samples, the maximum of the Seebeck coefficient *S* (and the *PF*) tends to be higher compared to pure $Bi_2Se_3$, although apparently shifted towards higher temperatures (Figs. 9 and 12). Namely, such a shift of the S-maximum towards higher temperatures is linked to an increase of the FC concentration and decrease of S in ordinary systems.

We believe this can be a rather common effect associated with the TM doping of chalcogenide materials with a small solubility of TM, as suggested in [43]. Since the nano-precipitates of varying size can better cover a larger area of the Fermi window [17-19] over monodispersed precipitates, such energy filtering can be optimized through a modification (e.g., kinetics) of the preparation route.

*3.3. Magnetic properties*

We make use of the magnetic measurements to corroborate the previous experiments and illuminate the nature of eventual precipitates. In summary, the MBE films of the Cr- doped $Bi_{2-x}Cr_xSe_3$ [10, 11] or Cr-intercalated ($Cr_xBi_2Se_3$) [12] $Bi_2Se_3$ has been studied. All papers report an unconventional FM ordering with maximum critical temperatures of 35 K for x=0.1 and 20 K for x=0.05. Contrarily, a tendency for AFM ordering has been reported for one substituted sample of a $Cr_{0.15}Bi_{1.85}Se_3$ single crystal [13]. This suggest that all forms of magnetism can appear within one single crystalline sample. The tendency towards clustering discussed above supports this conclusion in oversaturated materials. Namely, the concentration of Cr atoms can (i.e., will) vary spatially within a sample and even within a cluster. In such a case, the kinetics of sample preparation will play a major role next to thermodynamics, which otherwise would lead to equilibrium. The formation of misfit compounds reported in [16] may explain the diversity of the magnetic properties. Namely, the intralayer and interlayer interactions may produce FM and AFM ordering [16]. As a result, we find samples with various compositions within a single crystal. However, we expect to find homogeneous samples showing PM for much diluted $Bi_{2-x}Cr_xSe_3$ systems but find both AFM and FM ordering in samples that are forced to accumulate higher concentration of Cr. Indeed, the $Bi_{2-x}Cr_xSe_3$ samples with nominal x=0.005 and actual x=0.0025 show almost pure PM, indicating that chromium is truly dissolved in the matrix (Fig. 13). Even the magnetization curves show no trace of magnetic ordering. Instead, the magnetization saturates at high fields and perfectly matches the Brillouin function (Fig. 13 inset). We observe mostly the same picture for nominal x=0.01 and 0.02 (actual x=0.005 and 0.009). However, for nominal x≥0.02, the composition of the single-crystalline samples markedly varies within one batch, even for the materials prepared by FMC. Thus, two single-crystalline samples of one

batch generally show different magnetic properties and Cr contents. The analysis of the magnetic properties was as follows. First, we assume a quenching of the Cr orbital electron momentum (Cr is a *3d* element) [2]. Thus, the total momentum number *J* equals the spin momentum number *S*, *J*=*S*. We used magnetization-field data to fit the Brillouin function to obtain $J_{Brill}$ and the concentration of Cr atoms in the host matrix $n(Cr)_{Brill}$. We use the same $n(Cr)_{Brill}$ to fit the magnetization-temperature data with the Curie–Weiss (CW) law to acquire $J_{CW}$ for comparison. We used the CW law given by

$$\chi(T) = \frac{C}{T - T_{CW}} + \chi_0, \quad (2)$$

where $\chi$ is the magnetic susceptibility, *C* is the Curie constant, $T_{CW}$ is the critical paramagnetic temperature and $\chi_0$ is a temperature independent term that considers the mostly diamagnetic contributions of the host lattice. The Curie constant can be used to calculate $J_{CW}$ according to formula $C = n(Cr)g_J\mu_0\mu_B^2 J_{CW}(J_{CW}+1)$, where the Landé factor is $g_J$=2 for orbital quenching, and $\mu_0$and $\mu_B$ are the vacuum susceptibility and Bohr magneton, respectively. The parameters are summarized in Table 2.

This procedure produces a *J* that is slightly higher than the theoretical value of 1.5. This indicates the formation of both $Cr_{Bi}^{-1}$ (chromium effectively in the $Cr^{+2}$ state, *J*=2) next to $Cr_{Bi}$ (chromium effectively in the $Cr^{+3}$ state, *J*=1.5). This is in accordance with the Hall effect measurements, which reveal slight donor activity as discussed above. We assume the formation of a high spin in $Cr^{+2}$. Thus, the 4$^{th}$ unpaired electron of $Cr^{+2}$ moves to the $e_g$ orbital next to the 3 electrons in the $t_{2g}$ orbital, which is consistent with the weak-field Se matrix. Assuming the true substitutional solution (no clusters, $Cr_{Bi}$ only) of Cr in $Bi_2Se_3$ produces PM and that AFM/FM are the products of the compounds and clusters embedded in a single crystal, the maximum solubility is $x_{MAX}$ ≤0.003 (Table 2). We observe a strong inhomogeneity for the samples with a nominal x>0.02 accompanied by the formation of foreign phase of $Bi_2Cr_4Se_9$. Rather complex magnetic properties are observed for one sample $Bi_{2-x}Cr_xSe_3$ with a nominal x=0.04 (Fig. 14). While the high-temperature data CW fit gives a positive $T_{CW}$, i.e., an FM ordering, the CW fit of the low-temperature data gives a negative $T_{CW}$, i.e., an AFM ordering. Unfortunately, we observe no hysteresis in the magnetization data at any T to corroborate the FM ordering. We believe this is very soft material, i.e., the hysteresis lies within the measurement accuracy.

Such behavior can be explained by a partial occupation of the octahedral positions of the van der Waals gap by the Cr atoms. Such a partial occupation, 0.44 of the octahedral vdW positions, was described in the misfit-layer compounds from the Bi-Cr-Se system in [16]. In addition, such an accumulation of the manganese atoms in the vdW gap of the $Bi_2Te_3$ epitaxial layers was reported in [44]. According to the well-established Goodenough–Kanamori rule [e.g., 45], the exchange interaction of $Cr^{+3}$ ions (configuration $t_{2g}^3 - e_g^0$) coupled via Se atoms at 90° angle gives rise to FM ordering, which is the case for two Cr atoms in neighboring octahedral positions within the quintuple layer (QL) or vdW gap. On the other hand, the Cr-Se-Cr bridge at 180° allows the superexchange $t_{2g}^3 - t_{2g}^3$ interaction of $Cr^{+3}$ ions and is AFM in nature, which is the case for two Cr atoms within the QL or a lone Cr atom in the vdW gap coupled to Cr in place of Bi within the QL—compare the inset of Fig. 14. Thus, we have two competing interactions, FM and AFM, on the PM background of the diluted

Cr solid solution—a lone substitutional $Cr_{Bi}$ defect in the $Bi_2Se_3$ matrix (see inset in Fig. 14). We note that the mere occurrence of $Cr^{+2}$ (configuration $t_{2g}^3 - e_g^1$) facilitates FM ordering due to double exchange, i.e., due to real electron transfer among $Cr^{+3}$ and $Cr^{+2}$ ions. Interestingly, the $\chi$=f(T) is almost independent of the orientation, i.e., the results differ within measurement accuracy for in-plane and cross-plane magnetic field orientations. Such behavior is unexpected in a strongly anisotropic medium, although it is probably inherent to Cr in tetradymite crystals, as indicated by Cr-doped $Sb_2Te_3$ [2]. Strikingly, we observe the effect of the magnetic field strength (Fig. 14). Such a peculiar behavior calls for a thorough study on an even larger set of samples and is beyond the scope of this paper.

## 4. Conclusions

We prepared a series of $Bi_{2-x}Cr_xSe_3$ single crystals with a nominal x ranging between 0 and 0.04 in a near equilibrium state at T=823 K. The chromium decreases the total concentration of native defects. The true (substitutional) solubility of Cr in $Bi_2Se_3$ is x≤0.003 ($2x10^{19}$ Cr atoms per $cm^3$) at 820K. We assume the formation of nano-precipitates in the composition range (x=0.003–0.02), as the X-ray diffraction analyses indicate the presence of additional phases ($Bi_2Cr_4Se_9$) for x≥0.02. This conclusion is corroborated from the EDX/XRF analysis. The reciprocal space mapping reveals a modified mosaicity for the Cr-doped samples. We think the changes induced by the Cr doping lead to an extraordinary behavior of transport properties in $Bi_2Se_3$. The extraordinary behavior of the Seebeck coefficient and carrier mobility lead to an enhanced power factor in the doped crystals. In our view, this indicates the extraordinary energy filtering of free electrons. We suggest three possible mechanisms. First, the capture of electrons is due to the mixed valence state $Cr^{+2}/Cr^{+3}$. Further, the formation of Cr compound-based nano-precipitates leads to the energy dependent scattering of electrons. Finally, the modified mosaicity can induce a favorable energy filtering of electrons. For TE applications, further modifications of the preparation route would be beneficial in terms of optimizing the nano-structuring. A modified kinetics of the preparation may lead, for example, to a higher concentration of smaller inclusions. Furthermore, the TM induced mosaicity is expected to decrease the thermal conductivity, which is favorable for the ZT values. The magnetization data corroborates the picture drawn from the transport data. Furthermore, this indicates competing interactions of FM and AFM within the PM background of the diluted Cr solid solution in the $Bi_2Se_3$ matrix. Thus, it is worth exploring Cr-doped single crystals, especially in terms of the preparation route, as the kinetics and thermodynamics both play a role.

## Acknowledgments

The financial support from the Grant Agency of the Czech Republic (GA CR), project No. 16-07711S is greatly appreciated. V. H. acknowledges the support by the project NanoCent financed by the European Regional

Development Fund (ERDF, project No. CZ.02.1.01/0.0/0.0/15.003/0000485). K. P. appreciates support from the grants LM2015082, ED4.100/11.0251 and CZ.02.1.01/0.0/0.0/16_013/0001829 from the Ministry of Education, Youth and Sports of the Czech Republic.

**References**

[1] G. S. Nolas, J. Sharp, H. J. Goldsmid, Thermoelectrics, Basic Principles and New Materials Developments, Springer, Berlin, Heidelberg, 2001, p. 111.
[2] J. S. Dyck, C. Drasar, P. Lostak, C. Uher, Phys. Rev. B 71 (2005) 115214.
[3] V.A. Kulbachinskii, P.M. Tarasov, E. Bruck, Physica B 368 (2005) 32–41.
[4] V. A. Kulbachinski, P. M. Tarasov, and E. Brück, JETP Letters, Vol. 81, No. 7, (2005) 342–345.
[5] V. A. Kulbachinski, P. M. Tarasov, and E. Brück, Journal of Experimental and Theoretical Physics, Vol. 101, No. 3, (2005) 528–534.
[6] Y. S. Hor, P. Roushan, H. Beidenkopf, J. Seo, D. Qu, J. G. Checkelsky, L. A. Wray, D. Hsieh, Y. Xia, S.-Y. Xu, D. Qian, M. Z. hasan, N. P. Ong, A. Yazdani, and R. J. Cava, Phys. Rev. B 81 (2010) 195203.
[7] H. Yhang, C.-X. Liu, X.-L. Qi, Y. Fang and S-C. Yhang, Nat. Phys. 5 (2009) 438.
[8] Y. L. Chen, J.G. Analytis, J.-H. Chu, Z. K. Liu, S.-K. Mo, X. L. Qi, H. J. Zhang, D. H. Lu, X. Dai, Z. Fang, S. C. Zhang, I. R. Fisher, Z. Hussain, Z.-X. Shen, Science 325 (2009) 178.
[9] K. Kuroda, M. Arita, K. Miyamoto, M. Ye, J. Jiang, A. Kimura, E. E. Krasowskii, E. V. Chulkov, H. Iwasawa, T. Okuda, K. Shimada, Y. Ueda, H. Namatame, and M. Taniguchi, Phys. Rev. Lett. 105 (2010) 076802.
[10] 7.X. F. Kou, W. J. Jiang, M. R. Lang, F. X. Xiu, L. He, Y. Wang, X. X. Yu, A. V. Fedorov, P. Zhang, and K. L. Wang, J. Appl. Phys. 112 (2012) 063912
[11] M. Liu, J. Zhang, C.-Z. Chang, Z. Zhang, X. Feng, K. Li, K. He, L.-L. Wang, X. Chen, x. Dai, Z. Fang, Q.-K. Xue, X. Ma, and Y. Wang, Phys. Rev Lett. 108 (2012) 036805
[12] P. P. J. Haazen, J.-B. Laloe, T. J. Nummy, H. J. M. Swagten, P. Jarillo-Herrero, D. Heiman, and J. S. Moodera, Appl. Phys. Lett. 100 (2012) 082404.
[13] Y. H. Choi, N. H. Jo, K. J. Lee, J. B. Yoon, C. Y. You, and M. H. Jung, J. Appl. Phys. 109 (2011) 07E312 .
[14] J.-M. Zhang, W. Ming, Z. Huang, G.-B. Liu, X. Kou, Y. Fan, K. L. Wang, and Y. Yao, Phys. Rev. B 88 (2013) 235131.
[15] G. G. Shabunina, E. V. Kireeva, T. G. Aminov, Russ. J. Inorg. Chem. 41 (1996) 1496.
[16] S. M. Clarke and D. E. Feedman, Inorg. Chem. 54 (2015) 2765.
[17] J.-H. Bahk, Z. Bian, M. Zebarjadi, P. Santhanam, R. Ram, Appl. Phys. Lett. 99 (2011) 072118.
[18] S. V. Faleev,and F. Leonard, Phys. Rev. B 77 (2008) 214304.
[19] D. Narducci, E. Selezneva, G. Cerofoliny, S. Frabboni, G. Ottaviani, J. Solid State Chem. 193 (2012) 19.
[20] R. D. Shannon, Acta Crystallographica A32 (1976) 751.
[21] S. Nakajima, J. Phys. Chem. Solids 24 (1963) 479.
[22] U. Pietsch, V. Holy and T. Baumbach, *High-Resolution X-Ray Scattering From Thin Films to Lateral Nanostructures* (Springer-Verlag, Berlin, Heidelberg, New York 2004).
[23] H. Steiner, V. Volobuev, O. Caha, G. Bauer, G. Springholz and V. Holy, J. Appl. Cryst. 47 (2014) 1889.
[24] Drouin, D., Couture, A. R., Joly, D., Tastet, X., Aimez, V. and Gauvin, R. (2007). Scanning 29 (2007) 92.
[25] M. Balkanski R. F. Wallis, Semiconductor Physics and Applications, Oxford University Press, Oxford, 2000, p. 190-191.
[26] V. A. Kulbachinskii, N. Miura, H. Nakagawa, H. Arimoto, T. Ikaida, P. Lostak, C. Drasar, Phys. Rev. B 59 (1999) 15733.
[27] P. Ruleova, C. Drasar, A. Krejcova, L. Benes, J. Horak, P. Lostak, J. Phys. Chem. Solids 74 (2013) 746.
[28] J. P. Heremans, V. Jovovic, E. S. Toberer, A. Saramat, K. Kurosaki, A. Charoenphakdee, S. Yamanaka, G. J. Snyder, Science 321 (2008) 554.
[29] V.A. Kulbachinskii, N.B. Brandt, P.A. Cheremnykh, S.A. Azou, J . Horak, and P. Lostak, phys. stat. sol. (b) 160 (1988) 237-243.

[30] V. A. Kulbachinskii, H. Negishi, M. Sasaki, Y. Giman, M. Inoue, P. Lostak, and J. Horak, phys. stat. sol. (b) 199 (1997) 505-513.
[31] C.M. Jaworski, V. Kulbachinskii, J.P. Heremans, Phys. Rev. B 80 (2009) 233201.
[32] V. A. Kulbachinskii, V. G. Kytin, P. M. Tarasov, and N. A. Yuzeeva, Physics of the Solid State, Vol. 52, No. 9, (2010) 1830–1835.
[33] V. A. Kulbachinskii, N. Miura, H. Arimoto, T. Ikaida, P. Lostak, J. Horak, and C. Drasar, J. Phys. Soc. Japan 68 (1999) 3328.
[34] N. Cheng, R. Liu, S. Bai, X. I. Chen, J. Appl. Phys. 115 (2014) 163705.
[35] C. M. Bhandari, D. M. Rowe, in CRC Handbook of Thermoelectrics, ed. by D. M. Rowe (CRC Press, New York, 1994) p. 49.
[36] P. Lostak, L. Benes, S. Civis, H. Sussmann, J. Mater. Sci. 25 (1990) 277.
[37] P. Lostak, C. Drasar, I. Klichova, J. Navratil, T. Cernohorsky, Phys Status Solidi B 200 (1997) 289.
[38] V. A. Kulbachinskii, N. Miura, H. Nakagawa, H. Arimoto, T. Ikaida, P. Lostak, and C. Drasar, Phys. Rev. B, 59 (1999) 15733.
[39] P. Ruleova, C. Drasar, A. Krejcova, L. Benes, J. Horak, P. Lostak, J. Phys. Chem. Solids 74 (2013) 746.
[40] J. Kossut, phys. stat. sol.(b) 72 (1975) 359.
[41] G. Min, J. Electron. Mater. 39 (2010) 2459.
[42] D. Parker and D. Singh, Phys. Rev. B 85 (2012) 125209.
[43] J. Friedel, Can.J.Phys. 34 (1956) 1190.
[44] J. Ruzicka, O. Caha, V. Holy, H. Steiner, V. Volobuiev, A. Ney, G. Bauer, T. Duchon, K. Veltruska, I. Khalakhan, V. Matolin, E. F. Schwier, H. Iwasawa, K. Shimada and G. Springholz, New J. Phys. 17 (2015) 013028.
[45] J. S. Zhou and J. B. Goodenough, Phys. Rev. Lett. 96 (2006) 247202.

**Figures**

Fig. 1. XRD patterns of $Bi_{2-x}Cr_xSe_3$ single crystals for nominal x=0-0.04. There is clear evidence of an additional phase (peak at 2Θ = 31.3°) for x=0.03 and 0.04, which can be attributed to either $BiCrSe_3$ or $Bi_2Cr_4Se_9$. This peak is barely detectable for nominal x=0.02. The patterns are shifted vertically for clarity.

Fig. 2. Symmetric HR XRD scan of the $Bi_2Se_3$ and $Bi_{1.99}Cr_{0.01}Se_3$ single crystals (points) and the simulated curve (lines) using the crystallographic data of pure $Bi_2Se_3$ from [18]. The vertical lines denote the positions of the diffraction maxima 000L, the curves of the Cr-doped sample are shifted vertically for clarity.

Fig. 3. High-resolution XRD reciprocal-space maps measured around the 000.15 reciprocal-lattice points of the single crystals $Bi_{1.99}Cr_{0.01}Se_3$ (top panel) and $Bi_2Se_3$ (bottom). The color scale covers four decades of scattered intensity.

Fig. 4. The linear scans extracted from the reciprocal-space maps in Fig. 3 along the horizontal (a) and vertical directions (b). The arrows denote the features discussed in the text.

Fig. 5. XRF mapping of chromium (top) in the $Bi_2Cr_{0.01}Se_3$ BT grown single crystals (bottom; black rectangle corresponds to the analyzed area). The strong inhomogeneity in the Cr distribution is evident. Note that the Cr concentration increases towards the Bridgman crystal end (head), which indicates that the solubility of Cr is higher in the liquid phase than in the solid phase.

Fig. 6. The SEM/EDX mapping of chromium in $Bi_{2-x}Cr_xSe_3$ BT-grown single crystals.

Fig. 7. Electrical conductivity as a function of temperature for the $Bi_{2-x}Cr_xSe_3$ single crystals.

Fig. 8. Hall coefficient as a function of temperature for the $Bi_{2-x}Cr_xSe_3$ single crystals. The concentration of electrons n can be calculated using the following formula: $n=r_H/R_He$. The Hall factor $r_H$ is a constant for one particular temperature. Note that the very small difference in the effective mass (and thus mobility) of electrons in the two electron bands (discussed below) guaranties one can use this simple formula. Although

one would obtain $r_H \cong 0.8$ for acoustic phonons [25], we use $r_H=1$ to maintain the correspondence with the literature [e.g.26].

Fig. 9. Seebeck coefficient as a function of temperature for the $Bi_{2-x}Cr_xSe_3$ single crystals.

Fig. 10. Hall mobility as a function of temperature in a natural log-scale for the $Bi_{2-x}Cr_xSe_3$ single crystals. The solid line corresponds to scattering of acoustic phonons. Note that the scattering of acoustic phonons dominates above T=400 K, irrespective of the doping.

Fig. 11. a) Seebeck coefficient as a function of the Hall carrier concentration for $r_H=1$ (Pisarenko plot) for the $Bi_{2-x}Cr_xSe_3$ single crystals at T=450 K. Note that using $r_H=0.8$ (note at caption of Fig. 8) would shift the points towards lower carrier concentrations, but would not change the slope. The $\tau$ denotes samples annealed at920 K. Inset documents the depletion of the light electron (le) band upon decrease of the electron concentration. The heavy electron (he) band populated implies a rather higher Seebeck coefficient than predicted by the Pisarenko plot. This contradicts the experiment. b) The comparison of $Bi_{2-x}Cr_xSe_3$ with the $Bi_2Se_3$ single crystals doped with other elements showing the extraordinary behavior of Cr in the $Bi_2Se_3$ matrix. We quote the references in Section 3.2.

Fig. 12. Power factor as a function of temperature for the $Bi_{2-x}Cr_xSe_3$ single crystals.

Fig. 13. Susceptibility as a function of temperature for the $Bi_{2-x}Cr_xSe_3$ single crystal with a nominal x=0.005. The solid curve is a fit to the Curie–Weiss law. Inset: Magnetization as a function the magnetic field strength for the $Bi_{2-x}Cr_xSe_3$ single crystal with a nominal x=0.005. The solid curve represents the fit to the Brillouin function. The diamagnetic part proportional to field B was subtracted from the experimental values.

Fig. 14. Susceptibility as a function of temperature for the $Bi_{1.96}Cr_{0.04}Se_3$ single crystal for B=1 and 7 T. The solid lines are the fits according to the CW law. The outputs are summarized in Table 2. Inset: Three ways of embedding a small number of Cr atoms within the quintuple layers (QL) or between QL—in the vdW gap of $Bi_2Se_3$ leading to PM, FM, and AFM state—please compare with text.

**Table1**

Table 1. Comparison of nominal concentration of Cr with concentration obtained from XRF in $Bi_{2-x}Cr_xSe_3$ FCM grown single crystals with their transport and lattice parameters at 300 K. The difference between $x_{nom}$ and $x_{XRF}$ is due to segregation of Cr on the surface of bulk.

| nominal $x$ ($x_{nom}$) | $x_{XRF}$ | $\sigma$ ($10^5 \Omega^{-1}m^{-1}$) | $R_H$ ($cm^3C^{-1}$) | $n$ ($10^{19}cm^{-3}$) | $S$ ($\mu VK^{-1}$) | $a$ ($10^{-10}m$) | $c$ ($10^{-10}m$) | $V$ ($10^{-30}m^3$) |
|---|---|---|---|---|---|---|---|---|
| 0 | 0 | 2.54 | -0.270 | 2.31 | -59 | 4.1386 | 28.634 | 424.73 |
| 0.005 | 0.0025 | 2.37 | -0.318 | 1.96 | -60 | 4.1383 | 28.631 | 424.63 |
| 0.01 | 0.005 | 2.74 | -0.323 | 1.92 | -63 | 4.1378 | 28.631 | 424.51 |
| 0.02 | 0.009 | 2.26 | -0.451 | 1.38 | -66 | 4.1383 | 28.632 | 424.65 |
| 0.03 | 0.005 | 1.86 | -0.695 | 0.90 | -85 | 4.1372 | 28.627 | 424.34 |
| 0.04 | 0.019 | 1.53 | -0.949 | 0.66 | -91 | 4.1376 | 28.630 | 424.46 |

**Table2**

Table 2. Magnetic properties of $Bi_{2-x}Cr_xSe_3$ single crystals at B=1 T ($x_{Brill} \cong n_{Brill}/7.06 \cdot 10^{21}$ $cm^{-3}$). Brillouin function was used in fitting the experimental data measured at T=2 K. The total momentum number of Cr ion is calculated from Brillouin function $J_{Brill}$, and from Curie-Weiss law, $J_{CW}$. The data for x=0.04 could not be interpreted in terms of Brillouin function. Thus, the $J_{CW}$ is calculated using the $x_{XRF}$. Please, compare with Fig. 14. Note that the detection limit of Cr in XRF experiments is x≤0.001.

| nominal x | $x_{Brill}/x_{XRF}$ | $J_{Brill}/J_{CW}$ | $n(Cr)_{Brill}$ ($10^{19}cm^{-3}$) | $T_{CW}$ ( K ) | $\chi_0$ ($10^{-6}$) | Range fitted ( K ) |
|---|---|---|---|---|---|---|
| 0.005 | 0.001/0.0025 | 1.77/1.84 | 0.65 | -0.7 | 16.3 | 2-300 |
| 0.01 | 0.003/0.005 | 1.70/1.68 | 2.1 | 1.0 | 20.1 | 2-300 |
| 0.02 | 0.0026/0.009 | 1.71/1.74 | 1.83 | -0.5 | -2.9 | 2-300 |
| 0.04 LT | -/0.019 | -/2.0 | - | -4.0 | 132 | 2-45 |
| 0.04 HT | -/0.019 | -/2.3 | - | 60 | -16 | 100-300 |

Figure1

Click here to download Figure(s): Figure1_XRD.eps

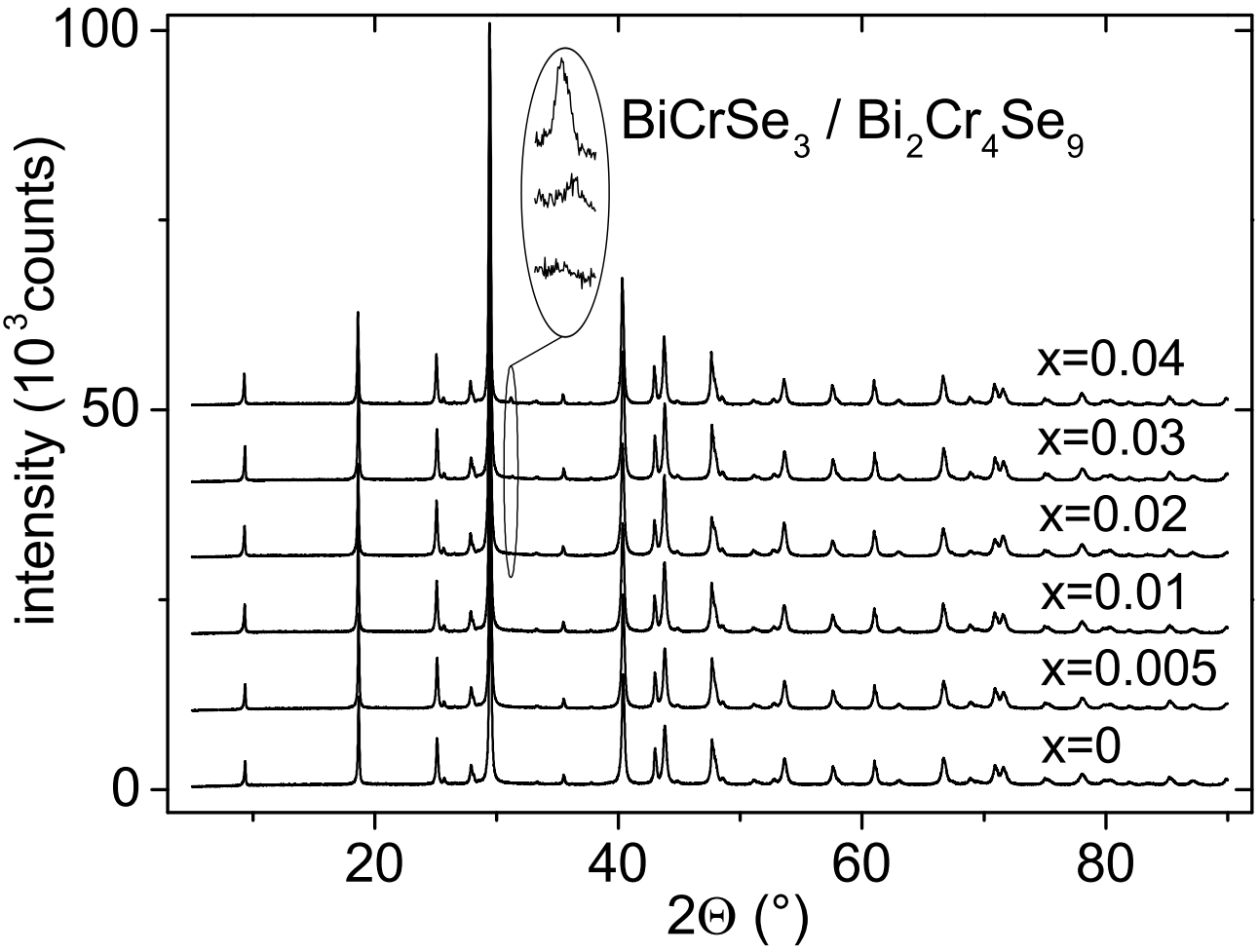

Figure2

Click here to download high resolution image

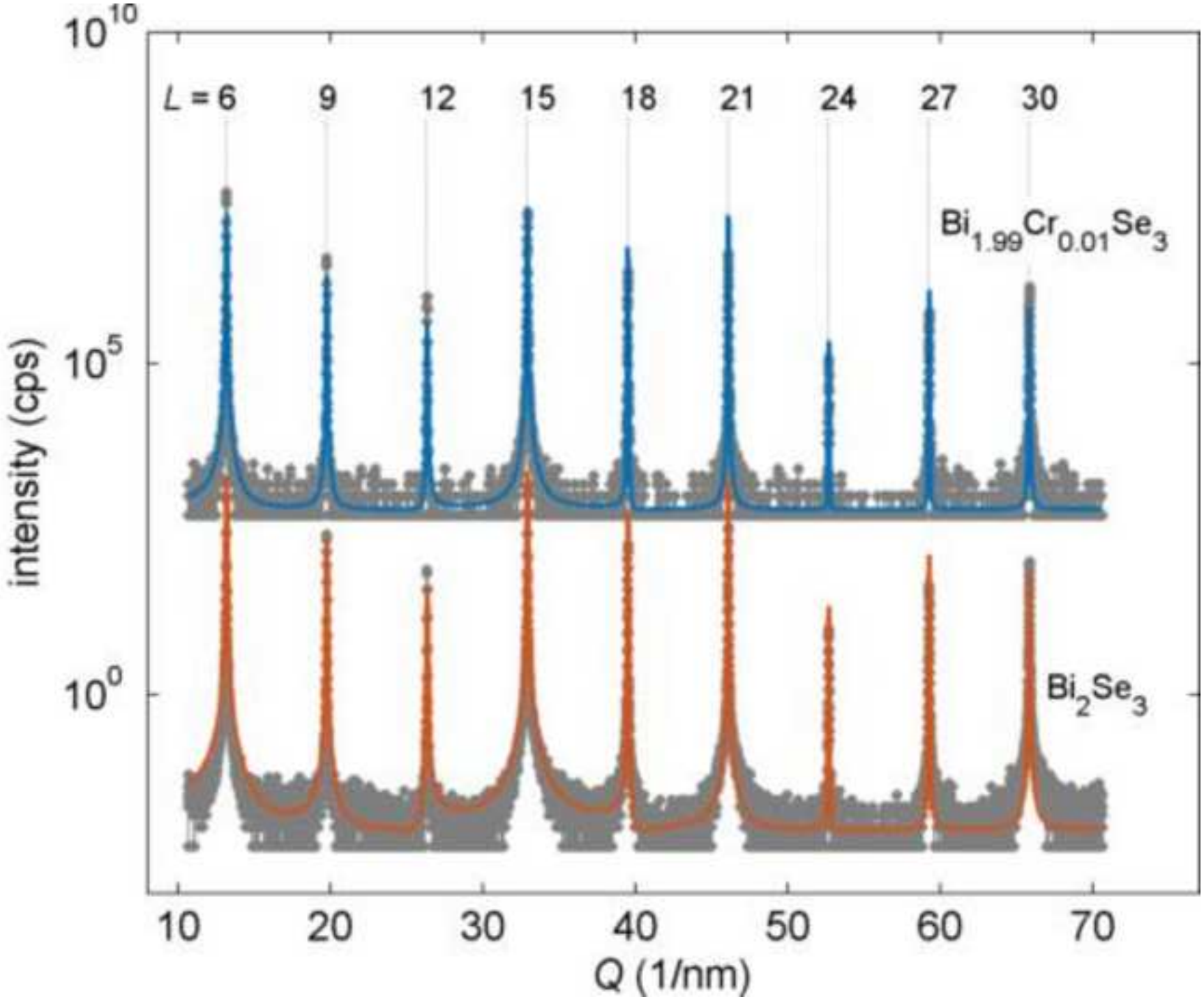

Figure3

Click here to download high resolution image

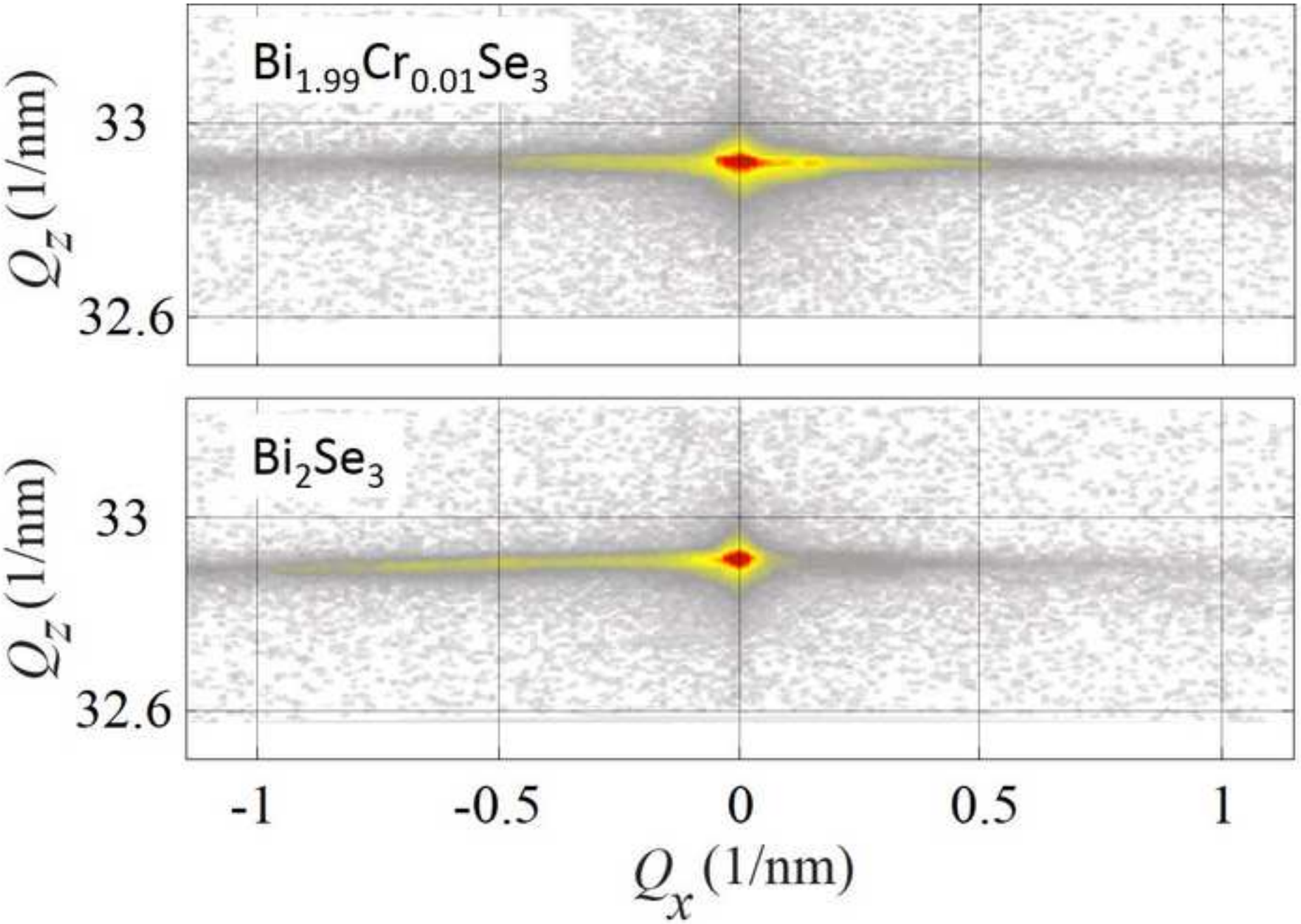

Figure4

Click here to download high resolution image

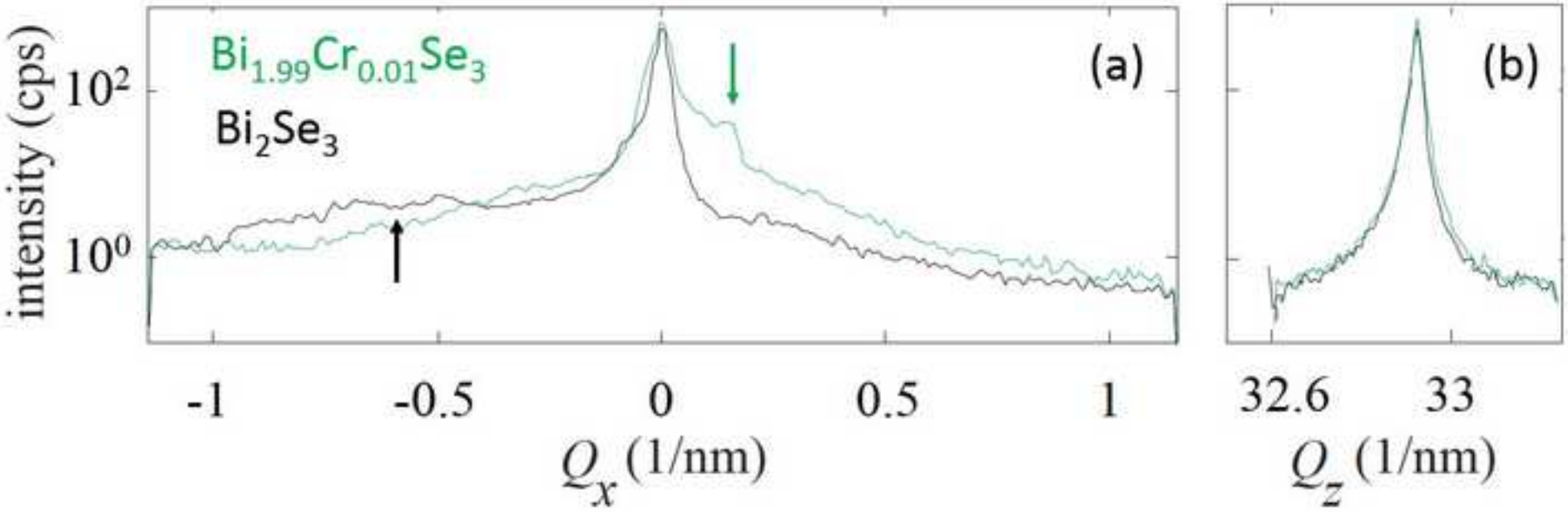

Figure5
Click here to download high resolution image

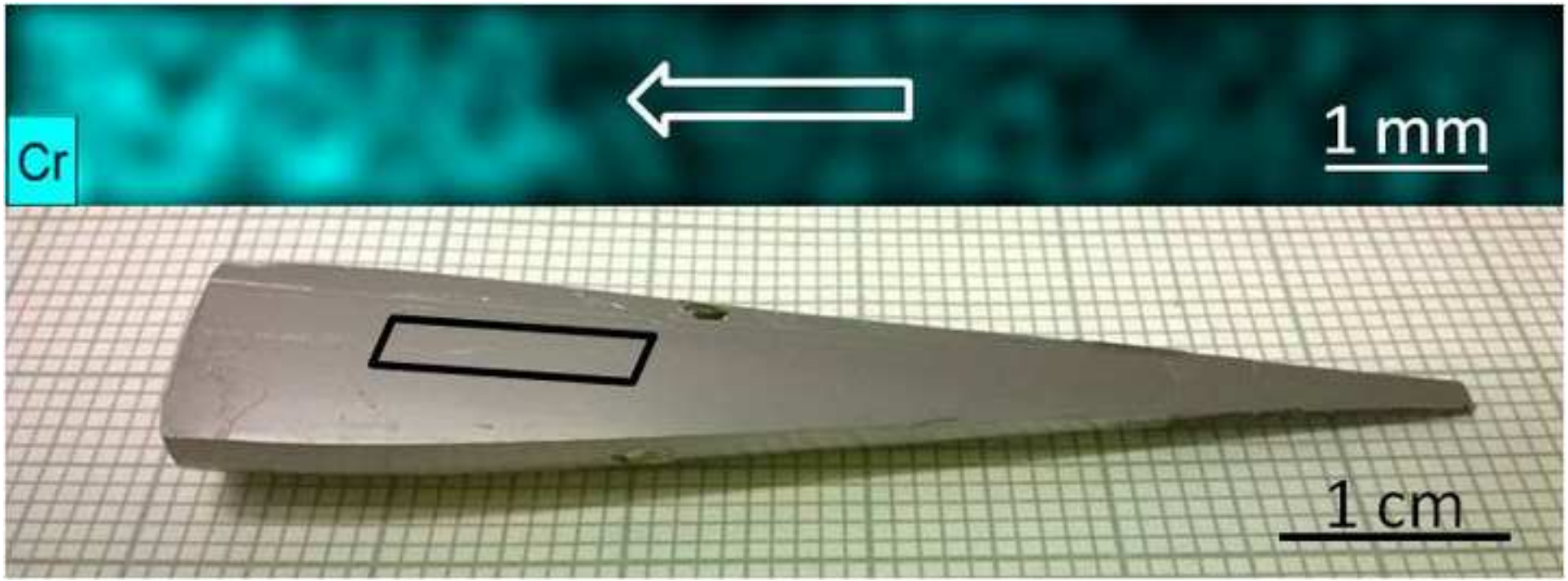

Figure6

Click here to download high resolution image

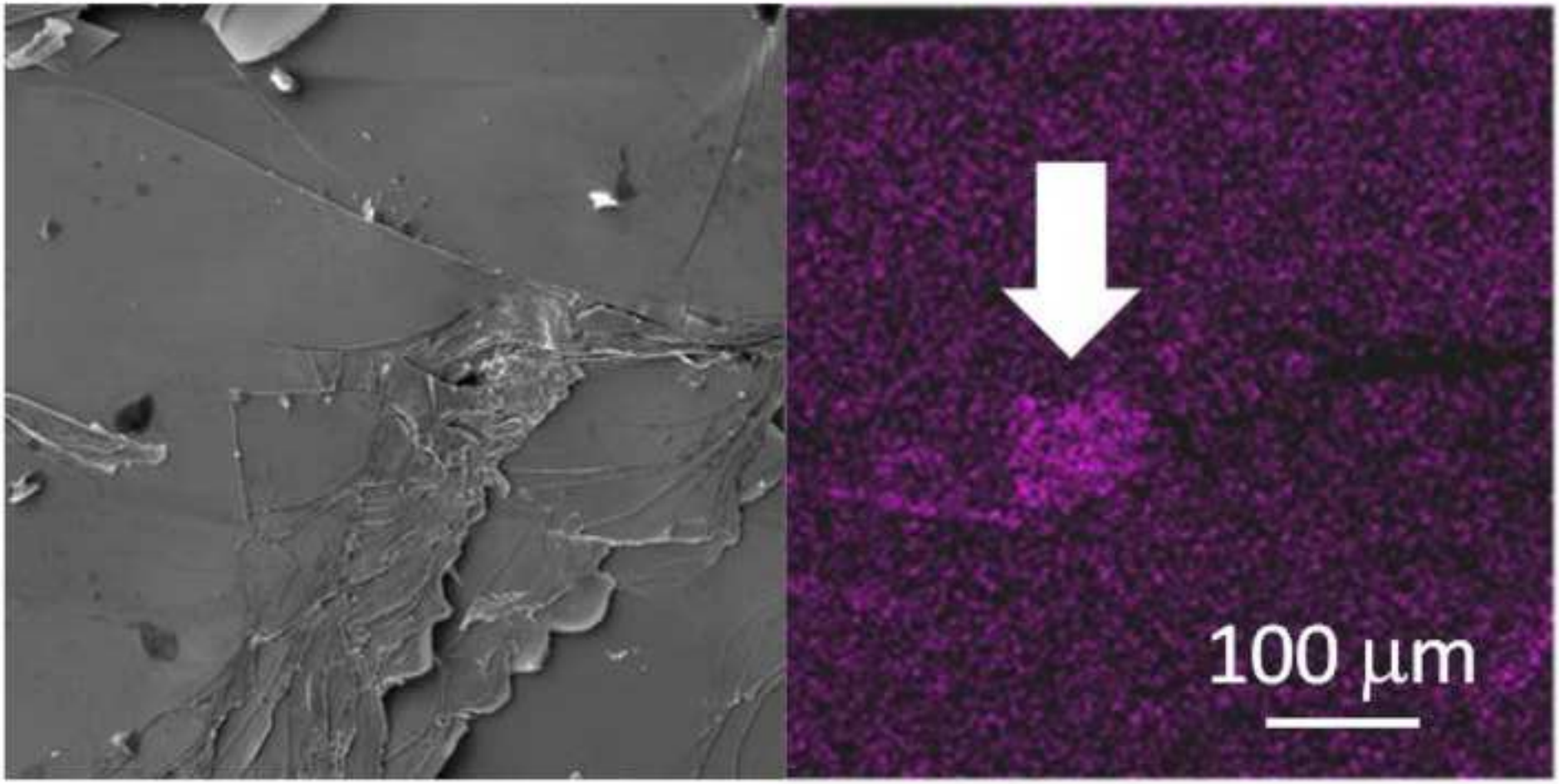

Figure7
Click here to download Figure(s): Figure7_Sigma.eps

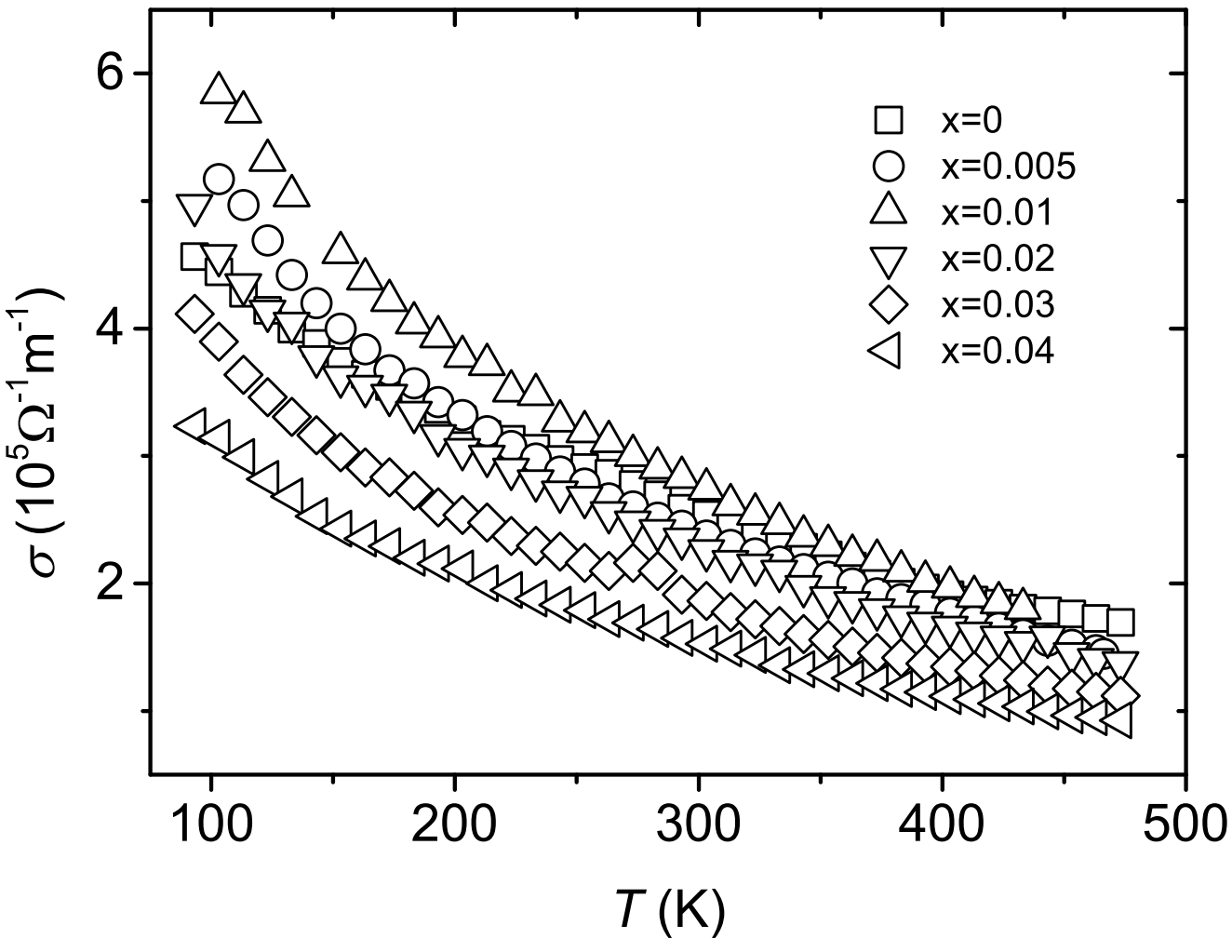

Figure8
Click here to download Figure(s): Figure8_Hall.eps

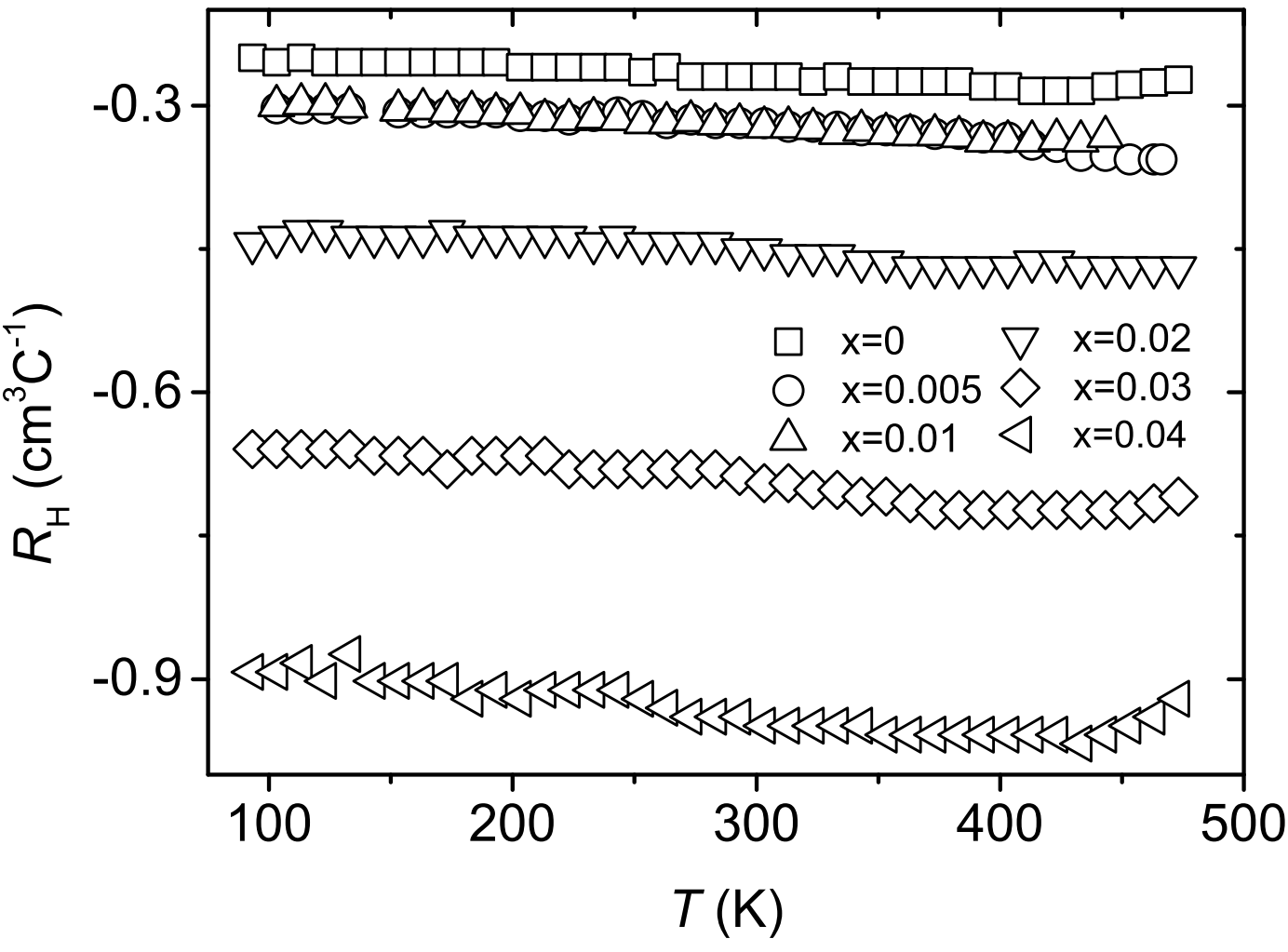

Figure9
Click here to download Figure(s): Figure9_Seebeck.eps

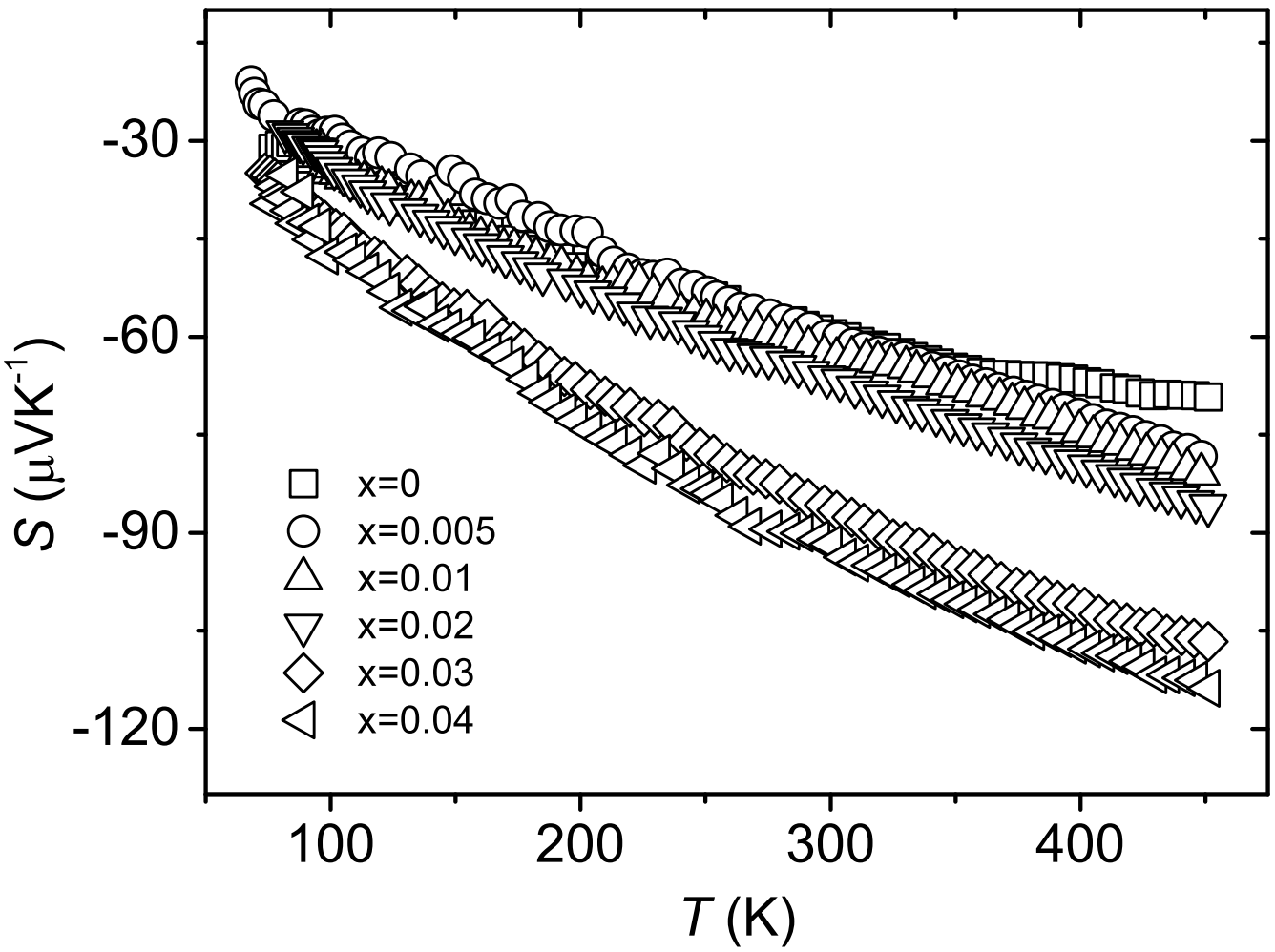

Figure10
Click here to download Figure(s): Figure10_Mobility.eps

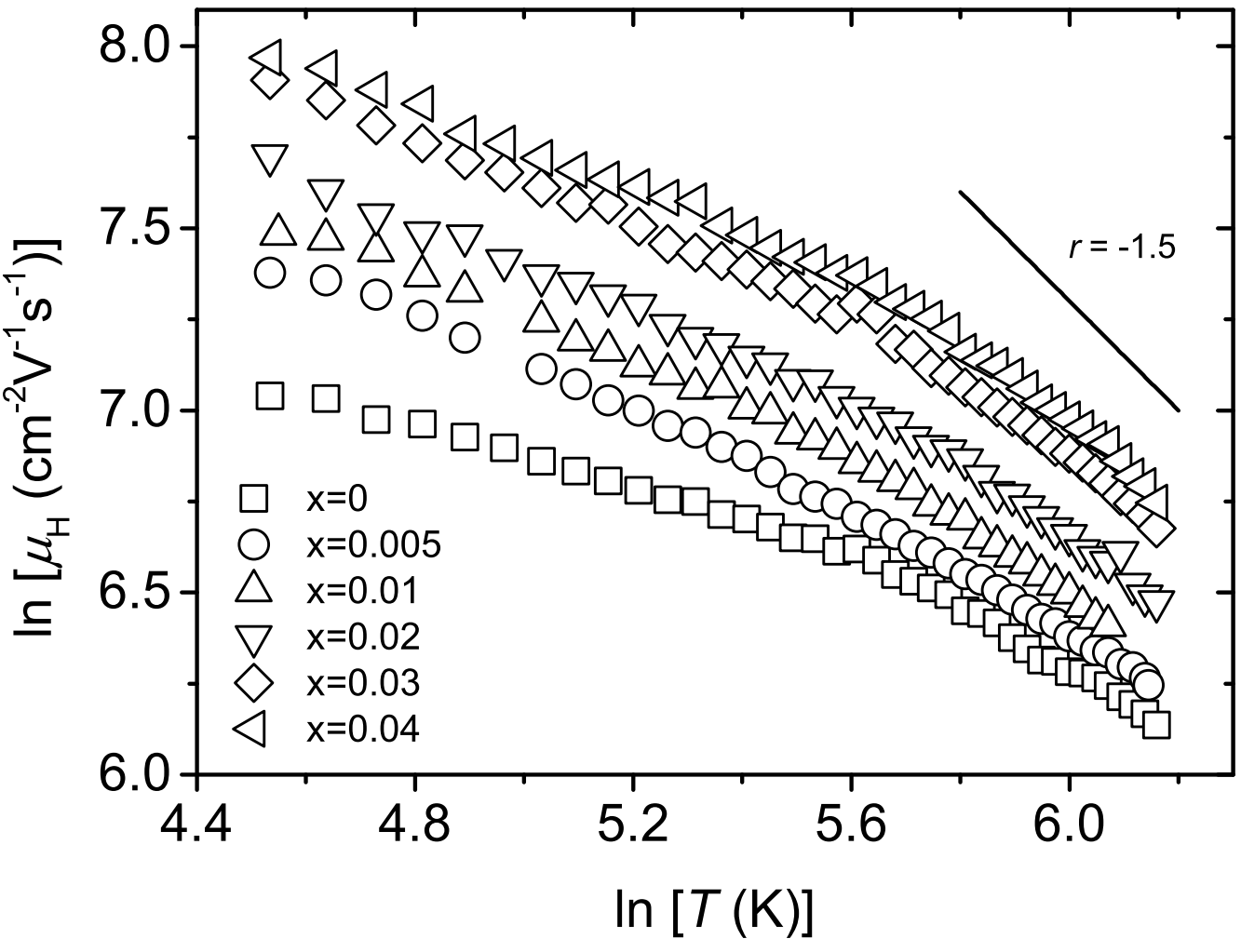

Figure11a

Click here to download Figure(s): Figure11a_Pisarenko.eps

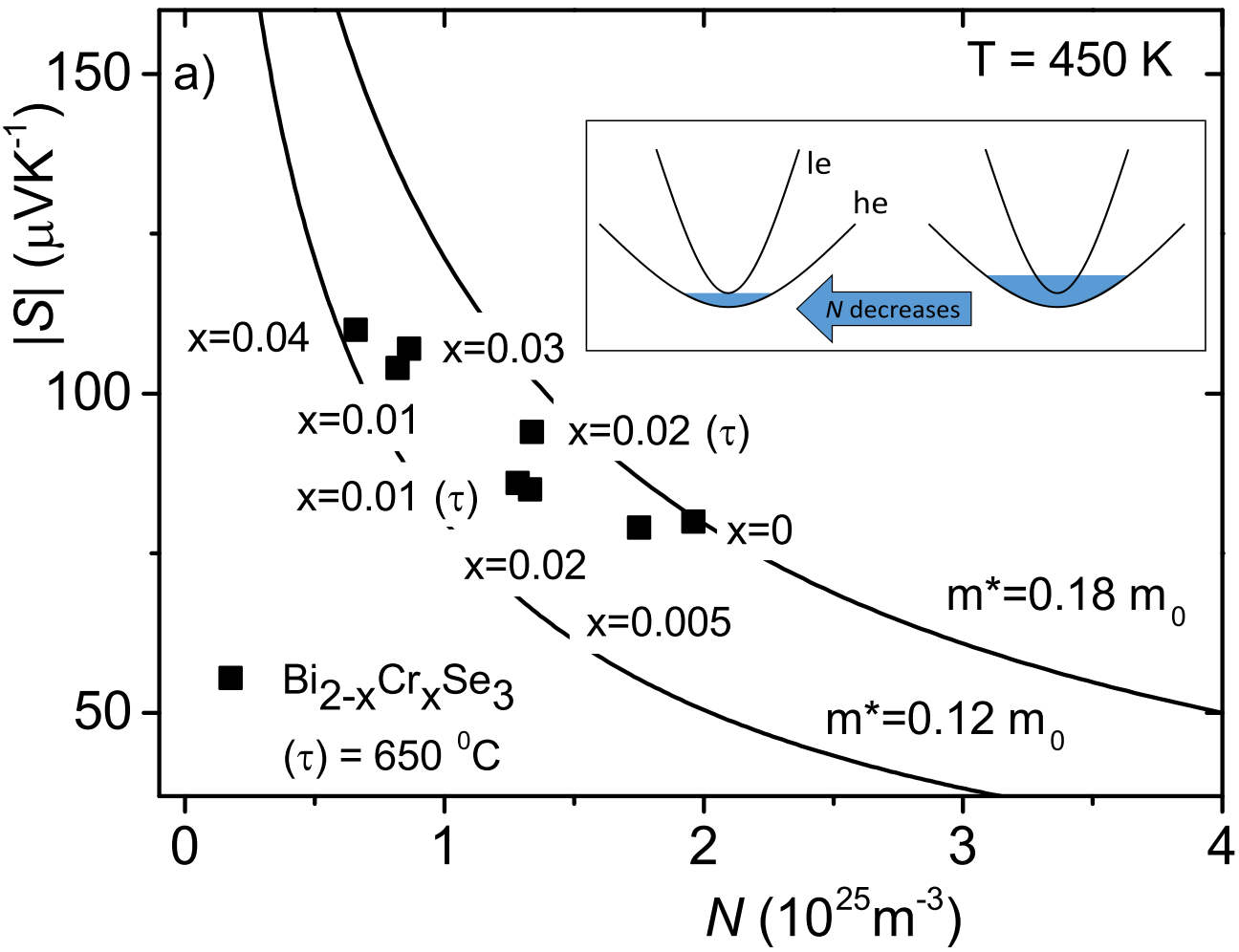

Figure11b
Click here to download Figure(s): Figure11b_Pisarenko.eps

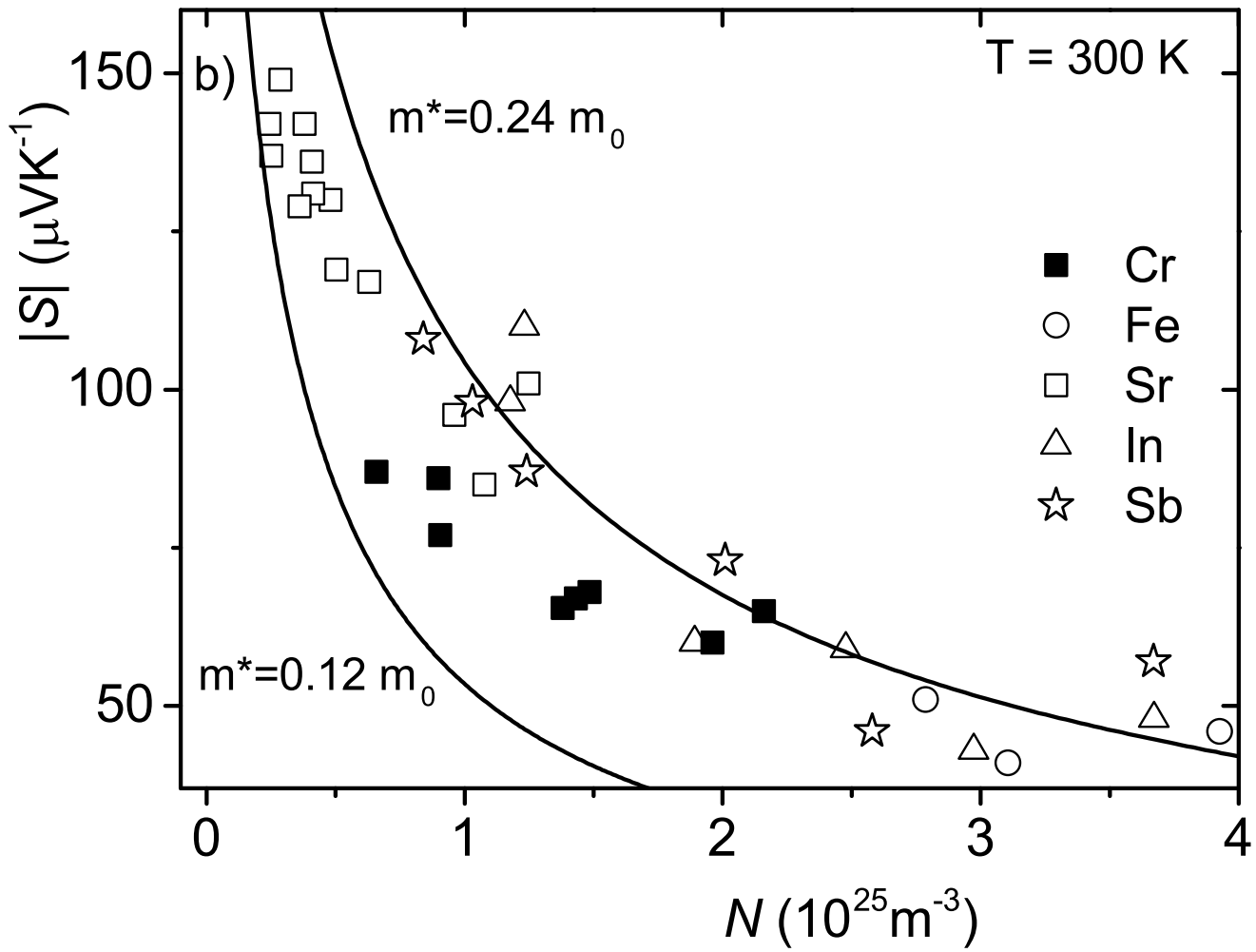

Figure12
Click here to download Figure(s): Figure12_PF.eps

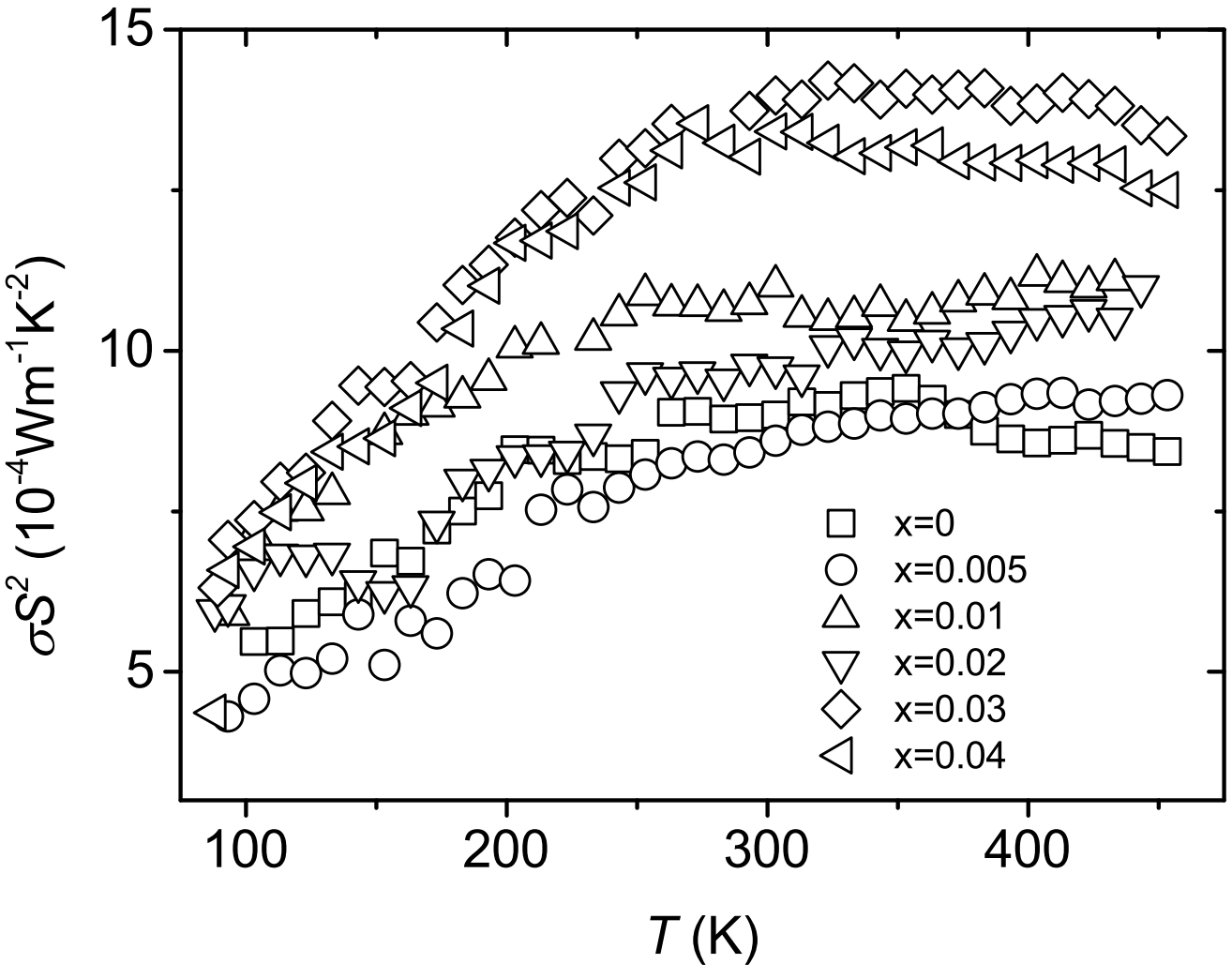

Figure13

Click here to download Figure(s): Figure13_Susceptibility_x005.eps

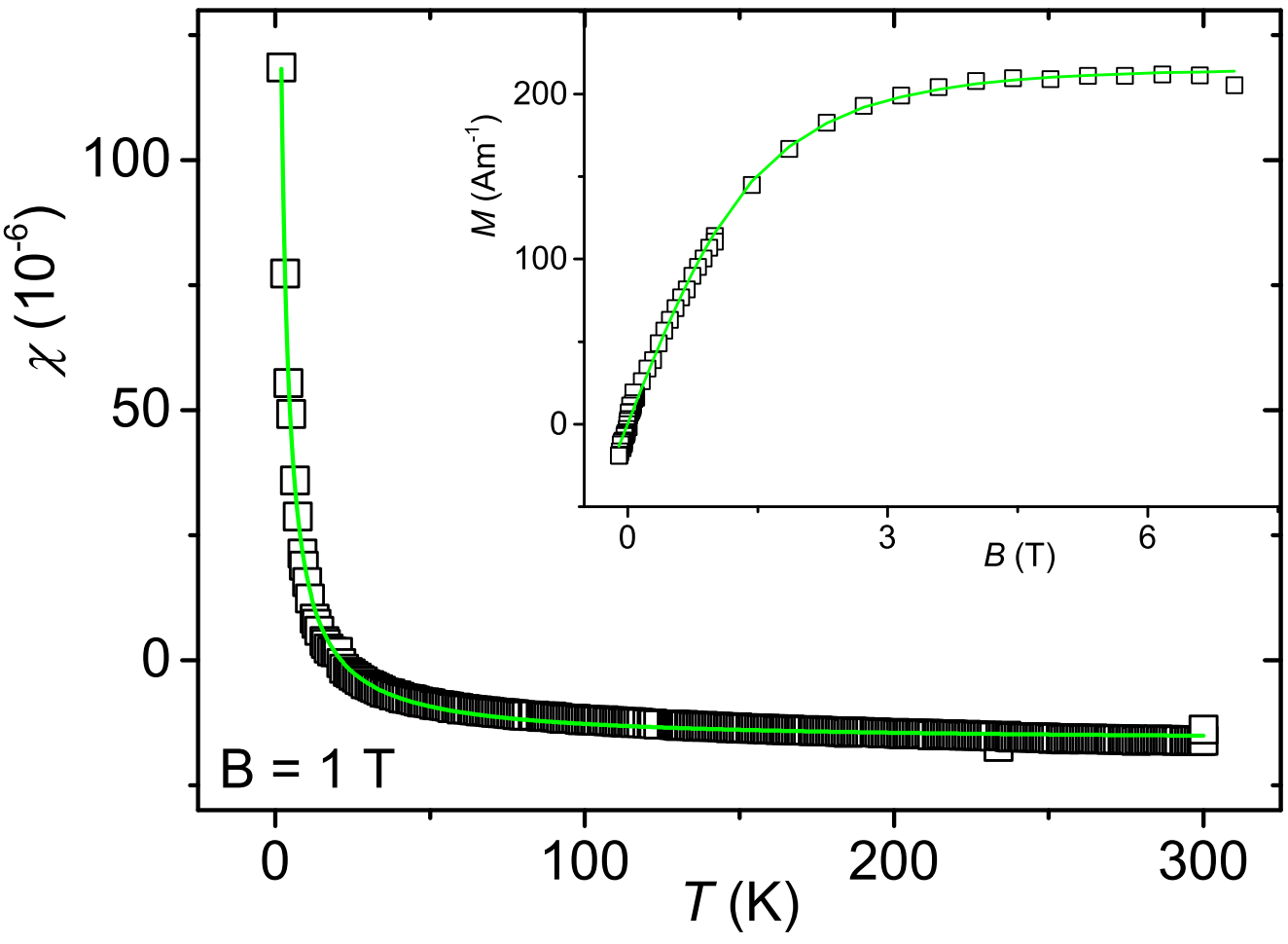

Figure14

Click here to download Figure(s): Figure14_Susceptibility_x04.eps

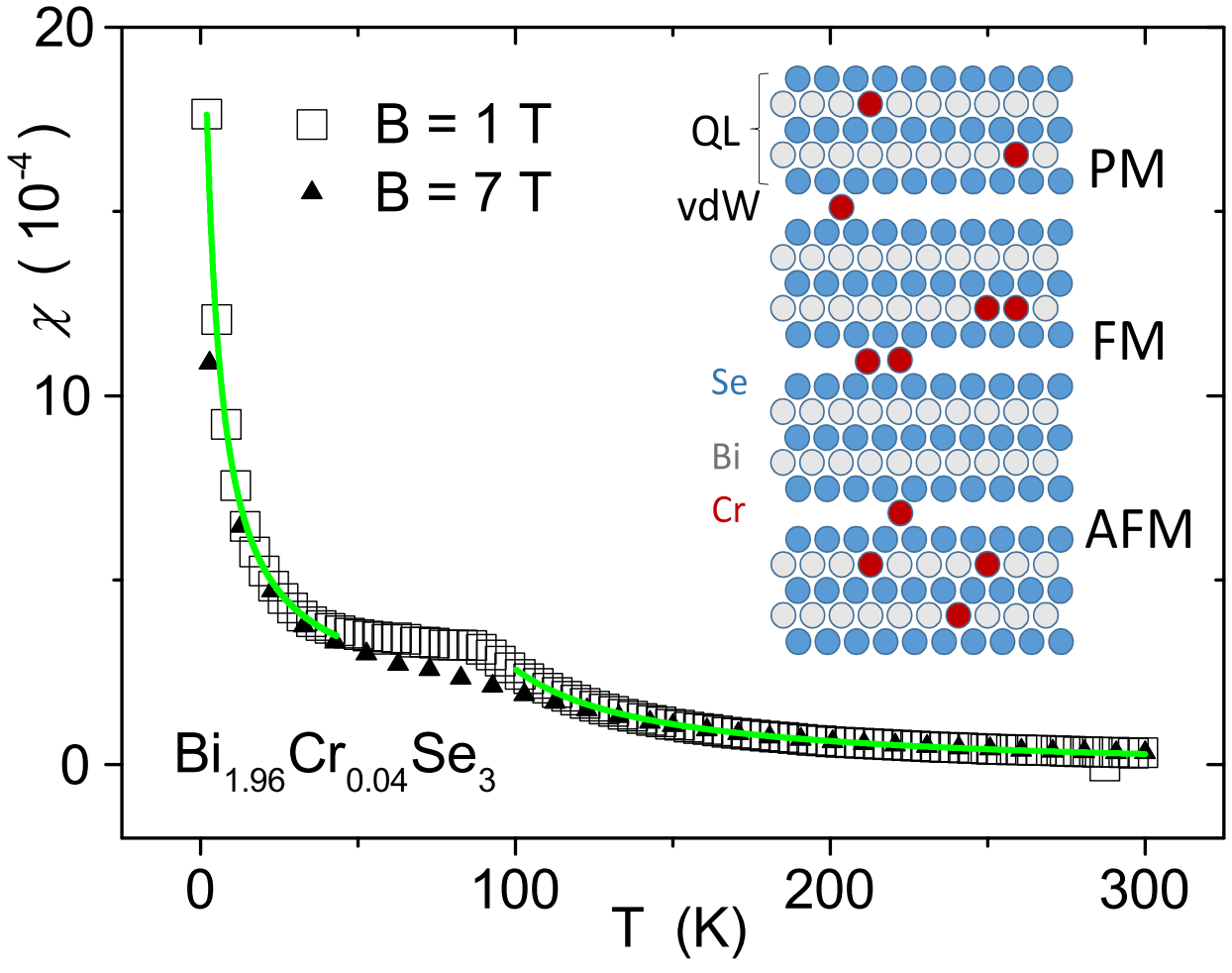

*Graphical Abstract

Click here to download high resolution image

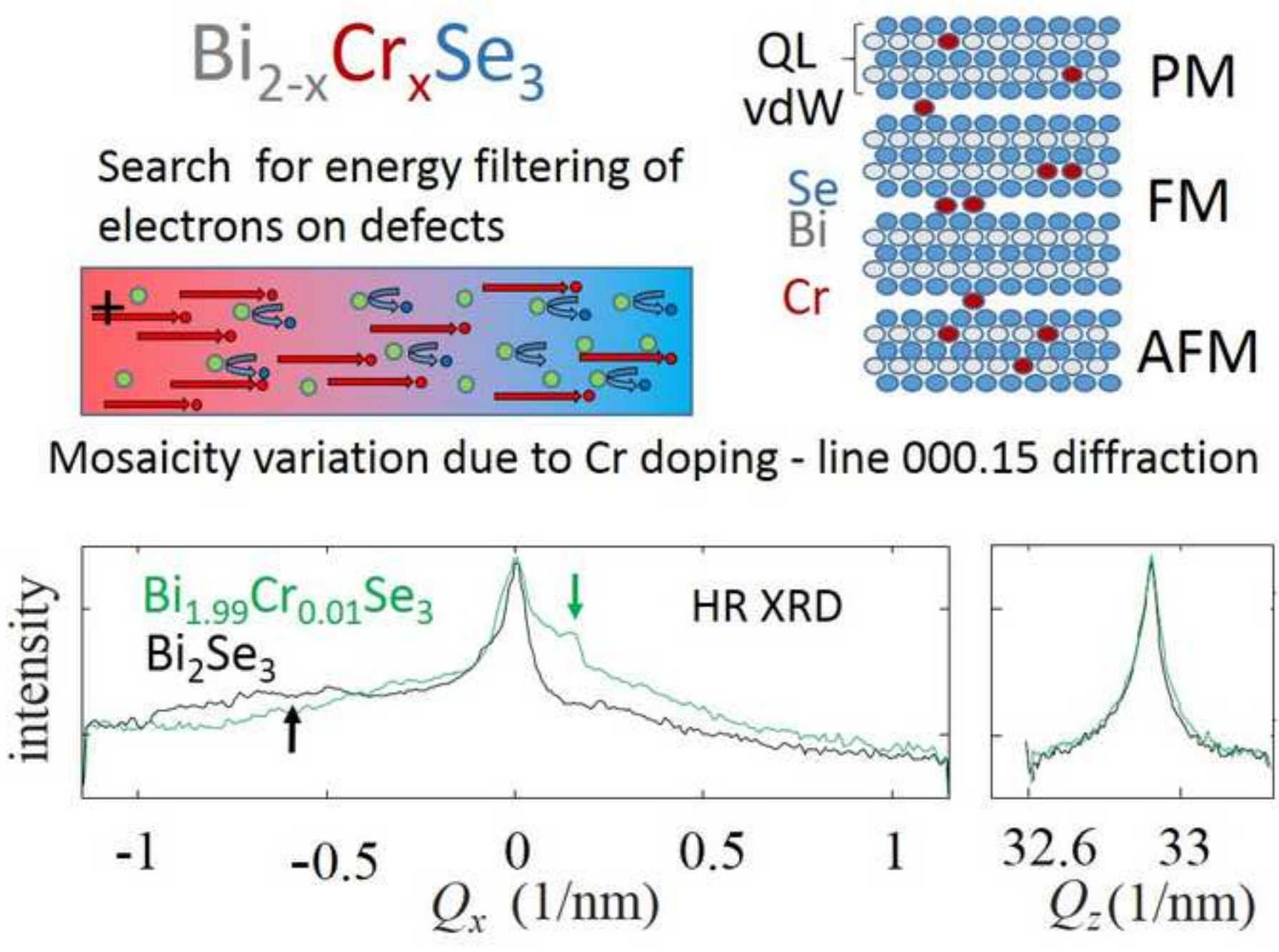

*Graphical Abstract Legend (TOC Figure)

Click here to download Graphical Abstract Legend (TOC Figure): Graphical_Abstract_Legend.docx

**Thermoelectric and magnetic properties of Cr-doped single crystal $Bi_2Se_3$ – search for energy filtering.**

**Highlights (for review)**

- Solubility of chromium is close to x=0.003 for $Bi_{2-x}Cr_xSe_3$ crystals
- Chromium doping varies mosaicity of $Bi_2Se_3$ single crystals.
- Chromium induces extraordinary behavior of physical parameters in $Bi_2Se_3$ crystals.
- Chromium doping seems to induce all forms of magnetism in $Bi_2Se_3$ crystals.